3-5-2007

Material Characterization Improvement in High Temperature Rectangle Waveguide Measurements

Eric A. Buschelman

MATERIAL CHARACTERIZATION IMPROVEMENT IN HIGH TEMPERATURE RECTANGULAR WAVEGUIDE MEASUREMENTS

THESIS

Eric A. Buschelman, Second Lieutenant, USAF

AFIT/GE/ENG/07-05

DEPARTMENT OF THE AIR FORCE
AIR UNIVERSITY

AIR FORCE INSTITUTE OF TECHNOLOGY

Wright-Patterson Air Force Base, Ohio

AFIT/GE/ENG/07-05

MATERIAL CHARACTERIZATION IMPROVEMENT IN HIGH TEMPERATURE RECTANGULAR WAVEGUIDE MEASUREMENTS

THESIS

Presented to the Faculty

Department of Electrical and Computer Engineering

Graduate School of Engineering and Management

Air Force Institute of Technology

Air University

Air Education and Training Command

In Partial Fulfillment of the Requirements for the

Degree of Master of Science in Electrical Engineering

Eric A. Buschelman, B.S.E.E.

Second Lieutenant, USAF

March 2007

AFIT/GE/ENG/07-05

MATERIAL CHARACTERIZATION IMPROVEMENT IN HIGH TEMPERATURE RECTANGULAR WAVEGUIDE MEASUREMENTS

Eric A. Buschelman, B.S.E.E.

Second Lieutenant, USAF

Approved:

Michael Havrilla	05 Mar 2007
Dr. Michael J. Havrilla (Chairman)	date
	3/5/2007
Dr. Andrew J. Terzuoli (Member)	date
Paul E Crittenden	3/5/2007
Dr. Paul E. Crittenden (Member)	date

AFIT/GE/ENG/07-05

Abstract

This research presents a method using modal analysis by which electromagnetic characterization of materials in a partially filled rectangular waveguide, having a single top air gap, can be accurately performed. Thermal expansion of waveguides commonly occurs during high-temperature measurements, resulting in air gaps between the sample and waveguide walls. Higher order modes are excited by the discontinuous geometry, which are not accounted for in most closed form extraction algorithms. A correction must be applied that considers the complex power transmitted and stored by higher-order modes, not merely the dominant mode. Characterization independent of sample distance from the calibration plane is also presented.

Expanding upon previous analysis of partially filled rectangular waveguides, a modal solution for a single air gap between the top of the material sample and the waveguide wall is developed. The analysis is performed on samples of dielectric to verify the method, and further tests are performed on magnetic shielding material. Boundary conditions between the empty and partially filled regions are formulated so it is only necessary to explicitly satisfy two of the existing three field components, the third being linearly dependent.

Calculation of the complex permittivity and permeability of magnetic shielding material, within 10% of the true value, was achieved by using less than 20 modes. Measurement improvement of real permittivity is the strongest feature of the algorithm. Modal corrections of samples converged slowly or not at all if a large air gap (> 90mils) was present, indicating the sensitivity of the solution. The inclusion of the calibration plane independence analysis greatly improved the level of performance of the modal correction. Results are presented in S-band and X-band, although the concept is applicable to all frequency bands.

Acknowledgements

Tremendous thanks go out to several people: My wonderful wife who always loved me and tried her best to keep me on track through these 18 months - you'll have many more chances in the future. To my son - you're so wonderful! How hard it was for me to leave the house for work when I wanted to spend time with you! Thank you for being so well behaved.

To Dr. Havrilla, my advisor and best professor, who put up with a lot of my procrastination, but was (and is) always patient with me, and made me realize the importance of thinking physically and caring about details. Thanks for the never-ending encouragement. The support of Dr. Crittenden was invaluable, and I owe a large part of this work to his guidance.

I am very appreciative for the enthusiastic support of my sponsors, Pete Munk and Rodney George. Their interest in this topic really kept me going during the final stretch. Charlie McNeely, the lab technician, was an invaluable resource in the latter half of this research, and I am very thankful for his assistance and friendship.

To Dr. Baldwin and Chaplain Srode, who arranged for Mass at AFIT every week - Thanks be to God! What a blessing that has been.

RJ Barton, who always challenged me to never give less than my very best. I've learned a lot from your dedication to excellence - thanks for keeping me honest.

Most of all, thanks be to God for all the blessings he has bestowed upon his unworthy servant. (*Lk* 17:10).

Eric A. Buschelman

Table of Contents

Page

List of Figures

List of Tables

List of Symbols

List of Abbreviations

MATERIAL CHARACTERIZATION IMPROVEMENT IN HIGH TEMPERATURE RECTANGULAR WAVEGUIDE MEASUREMENTS

I. Introduction

Electromagnetic characterization of materials quantifies the response to applied electric and magnetic fields through the use of the complex quantities permittivity (ϵ) and permeability (μ), respectively. The real part of each complex number is related to energy storage in the material, while the imaginary part accounts for conduction losses, manifested as thermal energy.

In applied electromagnetics, the parameters ϵ and μ are routinely sought by microwave engineers, since these parameters determine the behavior of fields. Materials can be either non-magnetic dielectrics or magnetic materials with both electric and magnetic losses. It is common for certain types of materials to be used to absorb and dissipate electromagnetic field energy, such as that transmitted by a radar. These shielding materials are effective at reducing the echo area or radar cross section (RCS) [20]. The materials used to achieve this reduction typically vary in weight, composition, effective frequency band, and durability, as well as method of application.

A highly relevant topic in RCS engineering is the reduction of scattering from the exhaust cavity of aircraft engines. Shaping, the primary tool for RCS reduction, cannot be used on existing legacy aircraft. Therefore, radar absorbing shielding material must be applied to needed areas. It is necessary that the absorber be able to withstand the extremely high temperatures of the exhaust environment, typically 2500° F, without performance degradation. Ceramic shielding material is commonly used, because of its durability under heat.

As mentioned before, knowledge of ϵ and μ of the shielding material is necessary to determine the response of the electromagnetic fields and the effective RCS, that is, whether the shielding material will meet the requirement for RCS reduction. Microwave measurements are used to calculate the electromagnetic parameters of heat-resistant ceramic shielding material, but must be performed at elevated temperatures to properly simulate the performance environment. This requirement introduces several complications into the measurement process, which would otherwise be trivial. Thermal expansion of the metal waveguide, which is normally greater than that of the ceramic shielding material, introduces air gaps between the sample and the waveguide walls, leading to the excitation of higher order modes; this situation will be referred to as a partially filled waveguide (PFW). If a gap is nonexistent, then the situation is a fully filled waveguide (FFW).

The use of closed form algorithms, such as Nicolson-Ross-Weir (NRW), does not account for the complex power loss to higher-order and evanescent modes [23, 27]. These must be considered if an accurate extraction is desired. Occasionally, due to the extreme heat or imprecise placement, the sample will shift longitudinally away from (or towards) the calibration plane, introducing a phase shift. If the phase shift is not compensated, an extraction of the electromagnetic parameters will be flawed. This thesis uses modal analysis techniques to overcome the problem of an air gap and is combined with a new method for reference plane independent measurements in a rectangular waveguide containing magnetic material.

1.1 Problem Statement

A need exists to accurately characterize magnetic shielding materials at extremely high temperatures. During high temperature tests, thermal expansion of the waveguide causes air gaps to form between the sample under test and the waveguide walls. This geometry scatters higher-order modes inside the waveguide, although all but the dominant TE_{10} mode quickly evanesce. However, each higher order mode transmits or stores a finite amount of complex power that does not propagate to the

receiving sensor inside the network analyzer. Therefore, characterization using the NRW algorithm with the standard reflection (S_{11}, S_{22}) and transmission (S_{21}, S_{12}) scattering (S) parameters yields inaccurate results [17, 21, 29]. In addition, the reflection measurements are extremely sensitive to the axial placement of the sample in the waveguide. Any displacement from the calibration plane along the waveguide axis incurs a two-way phase delay or advance which, without compensation, yields inaccurate results.

This thesis presents a mode-matching analysis using TM^y modes to model a PFW system containing a single air gap between the top of the sample and the waveguide. Theoretical S-parameters, namely S_{11}^{thy} and S_{21}^{thy}, are calculated and compared to the experimental S-parameters obtained from the network analyzer. A complex 2-D Newton-Raphson root search algorithm solves for the values of permittivity and permeability that minimize the difference, which are assumed to be the actual values of the material parameters. It is shown numerically to be sufficient to enforce continuity of two of the three transverse field components at the boundary between the empty and PFW regions.

To counteract the error introduced by shifting the sample in the waveguide, the respective forward and reverse theoretical S-parameters are multiplied together and compared to the experimental forward and reverse products. A complex 2-D Newton-Raphson root search algorithm iteratively solves for permittivity and permeability based on these new functions. This reference plane independent (RPI) formulation is based on the mode-matching technique described above.

The combination of these components (mode matching, RPI formulation, and use for magnetic materials) has not, to the best knowledge of the author, been presented before.

1.2 Scope

The standard industry method for materials characterization uses the microwave stripline. The availability of appropriately sized samples, as well as ease of use and performing calculations, contribute greatly to this fact. Other popular test mechanisms include the focused beam, cavity resonator, coaxial waveguide, and single-probe waveguide [21]. All of these methods can be applied in high temperature situations, and perhaps the focused beam system gives the best performance (no higher order modes are excited). Since this thesis presents a solution specifically for the rectangular waveguide, other test setups are not discussed. This exclusion is appropriate, since many facilities, including the sponsor of this research, do not possess every apparatus on this list.

In general, materials characterization will need to be performed across a wide range of frequencies. However, only S-band (2.6 - 3.95 GHz) and X-band (8.2 - 12.4 GHz) measurements are taken throughout this research. The mode-matching technique can easily be applied to rectangular waveguides at other frequency bands. Also, only air gaps in the y direction (short dimension) of the waveguide are addressed; this is the more dramatic problem, since the transverse TE_{10} **E**-field is non-zero at these gaps. For gaps in the x direction (long dimension), the tangential (and transverse) **E**-field is identically zero along the boundary, so small gaps have less effect on the measurement, at least for dielectrics [21].

1.3 Thesis Organization

Chapter 2 gives an overview of previous research done in the area of partially filled waveguides, and highlights the contributions of this work. Chapter 3 presents an review of electromagnetic field theory necessary for the research, including the use of vector potentials. The derivation of the mode-matching solution to the problem, as well as the inclusion of the reference plane independent analysis, is discussed in Chapter 4. Experimental results and error analysis are provided in Chapter 5, and

conclusions and recommendations are summarized in Chapter 6. The appendices contain the NRW algorithm and integral proofs of Chapter 4.

II. Previous Efforts

Microwave measurement problems considering partially filled waveguides have been thoroughly treated over the years. Several texts, such as those by Collin [10], Harrington [16] and Marcuvitz [22], address the issue to varying degrees of complexity. This chapter will review some of these methods.

2.1 Modal Methods

Wexler [28] has presented a general analysis of scattered modes in discontinuous waveguides, without regard to the type of fields present. Boundary conditions and continuity of transverse fields are satisfied by an infinite series of modes on each side of the obstacle or junction. As in this thesis, the objective is to determine the distribution of complex power among the the scattered modes. Wexler uses the orthogonality relation

$$\int_{CS} \mathbf{e}_n \times \mathbf{h}_m \cdot \hat{u_z} dCS = 0$$

on the non-degenerate modes. Although [28] mentions only PEC obstacles, the modal formulation may be used on dielectric and/or magnetic material obstacles as well.

The problem of finding cutoff frequencies in a waveguide partially filled with an exponentially varying dielectric has been addressed by Gonzalez [15]; his solution does not, however, explicitly solve for the propagation constants of higher order modes.

The problem discussed by Jarem *et al.* [19] is similar to that treated in this research, although with notable differences. Using TM^y modes, Jarem uses a method of moments analysis to calculate the theoretical reflection and transmission coefficients, and uses least-squares curve fitting to match them to the measured S-parameter data. The axial propagation wave number γ_{bn} is the solution of the eigenvalue equation

$$\begin{aligned} &\tfrac{\gamma_{z1n}}{\epsilon_{b1}} \tanh\left(\gamma_{z1n} d\right) = \tfrac{\gamma_{z2n}}{\epsilon_{b2}} \tanh\left(\gamma_{z2n}\left(d-b\right)\right) \\ &\gamma_{zin}^2 + \gamma_{bn}^2 + \omega^2 \epsilon_{bi} \mu_{bi} = 0, \quad i = 1, 2 \end{aligned} \tag{2.1}$$

where d is the sample thickness, b is the height of the waveguide, and γ_{zin} is the y-directed wave number in the partially filled region. The index $i = 1, 2$ refers the subregions of material (ϵ_1, μ_1) and (ϵ_2, μ_2) respectively. To satisfy boundary conditions between the FFW and PFW region, Jarem tries three methods: matching a single $\mathbf{E}$ and $\mathbf{H}$ component at the FFW/PFW interface; using Galerkin's method to match the inner products of the fields; and matching all transverse field components individually. Jarem chooses to continue with the first method, matching a single transverse component of $\mathbf{E}$ and $\mathbf{H}$. This choice is justified by both numerical cross-checks and a variational admittance expression which depends only on two transverse components. A more rigorous validation of this choice of boundary conditions is given in this research.

Similarly, Catala-Civera *et al.* [8] present a method for extracting complex permittivity of a dielectric using PFW theory. An uncertainty study of the procedure is also given. The material sample is discontinuous in $\hat{x}$ (i.e. long transverse dimension). An iterative material perturbation technique is used to search for the correct axial wave number γ of the PFW, using

$$\gamma - \gamma_0 = -j\omega \frac{\iint \left[(\Delta\epsilon - j\Delta\sigma)\, \mathbf{E} \cdot \mathbf{E}_0 - \Delta\mu \mathbf{H} \cdot \mathbf{H}_0 \right] dS}{\iint (\mathbf{E}_0 \times \mathbf{H} - \mathbf{E} \times \mathbf{H}_0) \cdot \hat{z}\, dS}$$

where $\Delta\epsilon$ and $\Delta\mu$ are the material perturbations and the subscript "0" refers to the unperturbed values [6,16]. Depending on the height of the material sample, the initial unperturbed material parameters those of either the empty or full waveguide. The uncertainty analysis revealed greater error for low-loss samples, as well as samples of short axial length. Additionally, the importance of precise sample alignment with the calibration plane is stressed.

Bogle [7] has also developed a similar solution to the partially filled waveguide characterization problem, although he uses a slightly different formulation. The PFW used in his analysis has left-right gaps, with the sample in the center. Havrilla has used

a perturbational method to compensate for small gaps in a PFW, but has included only the dominant TE_{10} mode in the solution, excluding higher-order modes [17].

2.2 Variational Methods

While modal methods can provide an exact solution for wave propagation in an partially filled waveguide, variational calculus may also be used to obtain an approximate solution. Berk [6] outlined a general variational procedure for obtaining the complex propagation coefficients in a waveguide partially filled with a dielectric slab. Collin and Vaillancourt [11] have successfully used the Rayleigh-Ritz method to obtain approximate eigenfunctions and eigenvalues in a waveguide partially filled with dielectric in the y-axis. The piecewise function $\kappa(y)$ corresponds to the electric permittivity ϵ as a function of position. The magnetic vector potential is equal to

$$\mathbf{A} = \hat{y} A_y = \hat{y} \sin\left(\frac{\pi x}{a}\right) \psi_{En}(y)\, e^{\pm \gamma z}$$

where $\psi_{En}(y)$ is one of infinitely many solutions of the Sturm-Liouville equation

$$\frac{d^2\psi_E}{dy^2} - \frac{1}{\kappa(y)}\frac{d\kappa}{dy}\frac{d\psi_E}{dy} + \left(\kappa k_0^2 - \frac{\pi^2}{a^2} + \gamma_z^2\right)\psi_E = 0$$

having corresponding eigenvalues γ_n^2. It can be shown that the solutions ψ_{En} form an orthogonal set with respect to the weighting function κ^{-1}. Additionally, the equation

$$\gamma^2 \int_0^b \frac{1}{\kappa(y)} \psi_E^2 dy - \int_0^b \left\{ \left(\frac{d\psi_E}{dy}\right)^2 - \left(\kappa k_0^2 - \frac{\pi^2}{a^2}\right)\psi_E^2 \right\} \frac{dy}{\kappa(y)} = 0, \quad \kappa(y) \neq 0 \quad (2.2)$$

is a variational expression for the true propagation constant γ^2 [2]. Collin proposes the set of eigenfunctions in the empty waveguide,

$$\phi_{En} = \sqrt{\frac{\epsilon_{on}}{b}} \cos\left(\frac{n\pi y}{b}\right), \quad n = 0, 1, 2... \quad (2.3)$$

where ϵ is Neumann factor, to use in the extremisation of (2.2). This method is used to match the tangential components of the fields at the junction between the empty and partially filled waveguide [11]. While this technique is by its nature approximate, it has the advantage of avoiding the solution of a transcendental equation.

The use of the Rayleigh-Ritz method was improved by Vander Vorst and Govaerts, who computerized the algorithm for use in a variation-iteration method [26]. The exact solution for wave propagation in a waveguide containing E-plane slabs of dielectric has been given by Gardiol [14].

2.3 Other Methods

Fehlen [13], also using a modal field expansion, developed a rigorous PFW analysis for samples in a coaxial test fixture, with future application to high-temperature measurements in mind.

Seeking to improve on the transmission/reflection method of materials characterization, Baker-Jarvis *et al.* developed an method to correct errors of the NRW algorithm (found in Appendix A) in low-loss samples with thicknesses approximately integer multiples of half-wavelengths [3]. Relevant to this thesis is the presentation of a family of equations that are independent with respect to both the reference plane and the sample thickness itself. These equations isolate the s-parameters in terms of other known quantities, to be used in a minimization equation as part of a root search for the correct permittivity. The paper does not test magnetic materials, and is specific to measurements using fully-filled waveguides.

Wilson [29] and Champlin [9] have analyzed the effect of an air gap on calculation of complex permittivity from transmission and reflection measurements. Wilson, using Wexler's formulation with a material slab discontinuity, successfully derived field expansions in the empty and PFW regions. It is suggested that a conducting paste be applied in the gap as a correction, and this is done with great success. However, such a solution is not applicable in a high-temperature PFW situation, since

the paste cannot withstand the high temperature [21]. Champlin, recognizing the difficulty of obtaining uniformity in the sample, gives an analytic correction for small gaps to be used in characterization of non-magnetic materials. He does not use modal analysis.

2.4 Summary

Notable contributions concerning microwave measurements of a PFW system were reviewed in this chapter. Several works have been published investigating different PFW scenarios, including those containing variable dielectric material. Solution techniques are commonly modal or variational, with computational results often given as verification.

III. Electromagnetics Fundamentals

An understanding of basic electromagnetics and guided wave theory is necessary to develop the solution for the problem at hand. Presented in this chapter is an explanation of vector potentials, the proper use as they pertain to field construction, and a review of guided wave theory as it pertains to this thesis. The analysis of this chapter borrows extensively from [4], [16] and [21]. A $e^{j\omega t}$ time dependence is assumed and suppressed throughout. Readers familiar with these texts may feel comfortable moving to the next chapter.

3.1 Maxwell's Equations

Electric and magnetic field behavior in simple media, defined as linear, isotropic, homogeneous, and dispersive, can be described by the coupled vector form of Maxwell's equations:

$$\nabla \times \mathbf{E} = -\mathbf{M} - j\omega\mathbf{B} \tag{3.1a}$$

$$\nabla \times \mathbf{H} = \mathbf{J} + j\omega\mathbf{D} \tag{3.1b}$$

$$\nabla \cdot \mathbf{D} = \rho_e \tag{3.1c}$$

$$\nabla \cdot \mathbf{B} = \rho_m \tag{3.1d}$$

The following auxiliary relations, also for propagation in simple media, apply,:

$$\mathbf{D} = \epsilon\mathbf{E} \equiv (\epsilon' - j\epsilon'')\,\mathbf{E} \tag{3.2a}$$

$$\mathbf{B} = \mu\mathbf{H} \equiv (\mu' - j\mu'')\,\mathbf{H} \tag{3.2b}$$

$$\mathbf{J} = \sigma\mathbf{E} \tag{3.2c}$$

where ω is the radian frequency, $\mathbf{E}$ and $\mathbf{H}$ are the electric and magnetic fields respectively, $\mathbf{B}$ is the magnetic flux density, $\mathbf{D}$ is the electric flux density, $\mathbf{J}$ is the electric current density, $\mathbf{M}$ is the magnetic current density, ρ_e is the electric charge density, ρ_m is the magnetic charge density, ϵ is the complex electric permittivity, μ is the complex

magnetic permeability, and σ is the conductivity of the material. The real and imaginary components of permittivity and permeability are denoted with single ($\prime$) and double ($\prime\prime$) prime notation, respectively. Relative electric permittivity ϵ_r (or magnetic permeability μ_r) is defined as the ratio of the material permittivity (permeability) to the permittivity (permeability) of free space,

$$\epsilon_r = \frac{\epsilon}{\epsilon_0}$$
$$\mu_r = \frac{\mu}{\mu_0}$$

Maxwell's equations describe the coupling of electric and magnetic fields as energy propagates in space or through a material. The constitutive parameters ϵ, μ, and σ determine the field response in the material to the application of an electromagnetic field [21]. The real and imaginary parts of ϵ and μ represent energy stored in the material and loss mechanisms of the material, respectively.

3.2 Vector Potentials

It is useful to define auxiliary functions to aid in the solutions of problems involving Maxwell's equations, such as the partially filled waveguide problem of this thesis.

3.2.1 Magnetic Vector Potential. The fields generated by an electric current in a region free of magnetic sources (i.e. $M = 0$) must satisfy Gauss's Law, $\nabla \cdot \mathbf{B} = 0$. Since in a source free region $\mathbf{B}$ is always solenoidal, this implies it has a magnetic vector potential $\mathbf{A}$, such that

$$\mathbf{B}_A = \nabla \times \mathbf{A} \tag{3.3}$$

or, by (3.2b),

$$\mathbf{H}_A = \frac{1}{\mu} \nabla \times \mathbf{A} \tag{3.4}$$

Substituting (3.4) into (3.1a) yields

$$\nabla \times \mathbf{E}_A = -j\omega\mu\mathbf{H}_A = -j\omega\nabla \times \mathbf{A} \tag{3.5}$$

which can also be written as

$$\nabla \times [\mathbf{E}_A + j\omega\mathbf{A}] = 0 \tag{3.6}$$

By identity, this implies that $\mathbf{E}_A + j\omega\mathbf{A}$ has a scalar potential, that is

$$\mathbf{E}_A + j\omega\mathbf{A} = -\nabla\phi_e \tag{3.7}$$

or,

$$\mathbf{E}_A = -\nabla\phi_e - j\omega\mathbf{A} \tag{3.8}$$

where the electric scalar potential ϕ_e is a function of position.

By taking the curl of both sides of (3.4) and using the vector identity $\nabla \times \nabla \times \mathbf{A} = \nabla(\nabla \cdot \mathbf{A}) - \nabla^2\mathbf{A}$, it can be reduced to

$$\mu\nabla \times \mathbf{H} = \nabla(\nabla \cdot \mathbf{A}) - \nabla^2\mathbf{A} \tag{3.9}$$

Using (3.1b) leads to

$$\mu\mathbf{J} + j\omega\epsilon\mu\mathbf{E}_A = \nabla(\nabla \cdot \mathbf{A}) - \nabla^2\mathbf{A} \tag{3.10}$$

Substituting (3.8) into (3.10) obtains

$$\nabla^2\mathbf{A} + k^2\mathbf{A} = -\mu\mathbf{J} + \nabla(\nabla \cdot \mathbf{A}) + \nabla(j\omega\epsilon\mu\phi_e) \tag{3.11}$$

$$= -\mu\mathbf{J} + \nabla(\nabla \cdot \mathbf{A} + j\omega\epsilon\mu\phi_e) \tag{3.12}$$

where $k^2 = \omega^2\epsilon\mu$. Having previously defined the curl of $\mathbf{A}$ in (3.3), the divergence of $\mathbf{A}$, which is independent of the curl, may be defined as

$$\nabla \cdot \mathbf{A} = -j\omega\epsilon\mu\phi_e \tag{3.13}$$

which is known as the Lorentz gauge condition. Substituting into (3.11) results in

$$\nabla^2\mathbf{A} + k^2\mathbf{A} = -\mu\mathbf{J} \tag{3.14}$$

This is known as the wave equation for $\mathbf{A}$. The electric vector field due to the magnetic vector potential $\mathbf{A}$, using (3.13) in (3.8), can be written as

$$\mathbf{E}_A = -\nabla\phi_e - j\omega\mathbf{A} = -j\omega\mathbf{A} + \frac{1}{j\omega\epsilon\mu}\nabla\left(\nabla \cdot \mathbf{A}\right) \tag{3.15}$$

Thus knowledge of $\mathbf{A}$ enables the finding of $\mathbf{E}_A$ and $\mathbf{H}_A$ from (3.15) and (3.4), respectively. The components of the fields due to an electric current density $\mathbf{J}$ having been found, it remains necessary to calculate the fields due to a magnetic current $\mathbf{M}$.

3.2.2 Electric Vector Potential. The fields generated by an equivalent magnetic current in a region free of electric sources (i.e. $J = 0$) must satisfy Gauss's Law, $\nabla \cdot \mathbf{D} = 0$. Observing that $\mathbf{D}$ is also solenoidal, this implies it has an electric vector potential $\mathbf{F}$ such that

$$\mathbf{D}_F = \nabla \times \mathbf{F} \tag{3.16}$$

or, by (3.2a),

$$\mathbf{E}_F = -\frac{1}{\epsilon}\nabla \times \mathbf{F} \tag{3.17}$$

Substituting (3.17) into (3.1b) yields

$$\nabla \times \mathbf{H_F} = j\omega\epsilon\mathbf{E}_F = j\omega\nabla \times \mathbf{F} \tag{3.18}$$

which can also be written

$$\nabla \times [\mathbf{H}_F + j\omega\mathbf{F}] = 0 \tag{3.19}$$

By identity, this implies that $\mathbf{H}_F + j\omega\mathbf{F}$ has a scalar potential, that is

$$\mathbf{H}_F + j\omega\mathbf{F} = -\nabla\phi_m \tag{3.20}$$

or

$$\mathbf{H}_F = -\nabla\phi_m - j\omega\mathbf{F} \tag{3.21}$$

where the magnetic scalar potential ϕ_m is a function of position.

By taking the curl of both sides of (3.17) and using the vector identity $\nabla \times \nabla \times \mathbf{F} = \nabla(\nabla \cdot \mathbf{F}) - \nabla^2\mathbf{F}$, it can be reduced to

$$-\epsilon\nabla \times \mathbf{E}_F = \left[\nabla(\nabla \cdot F) - \nabla^2 F\right] \tag{3.22}$$

Using (3.1a) leads to

$$\epsilon\mathbf{M} + j\omega\epsilon\mu\mathbf{H}_F = \nabla(\nabla \cdot F) - \nabla^2 F \tag{3.23}$$

Substituting (3.21) into (3.23) obtains

$$\nabla^2\mathbf{F} + k^2\mathbf{F} = -\epsilon\mathbf{M} + \nabla(\nabla \cdot \mathbf{F} + j\omega\epsilon\mu\phi_m) \tag{3.24}$$

Having previously defined the curl of $\mathbf{F}$ in (3.16), the divergence of $\mathbf{F}$, which is independent of the curl, may be defined as

$$\nabla \cdot \mathbf{F} = -j\omega\epsilon\mu\phi_m \tag{3.25}$$

which is known as the Lorentz gauge condition. Substituting this into (3.24) results in

$$\nabla^2\mathbf{F} + k^2\mathbf{F} = -\epsilon\mathbf{M} \tag{3.26}$$

This is the wave equation for $\mathbf{F}$. The magnetic vector field due to the electric vector potential $\mathbf{F}$, using (3.25) in (3.21) can be written as

$$\mathbf{H}_F = \frac{1}{j\omega\epsilon\mu}\nabla\left(\nabla\cdot\mathbf{F}\right) - j\omega\mathbf{F} \tag{3.27}$$

Thus knowledge of $\mathbf{F}$ enables the determination of $\mathbf{E}_F$ and $\mathbf{H}_F$ from (3.17) and (3.27), respectively.

3.2.3 Summary. It has been shown that the electromagnetic field components sustained by an electric current density $\mathbf{J}$ or magnetic current density $\mathbf{M}$ can be calculated through use of the magnetic vector potential $\mathbf{A}$ or electric vector potential $\mathbf{F}$. When both sources are present, the principle of superposition may be applied to determine the total fields, namely

$$\mathbf{E}_{total} = \mathbf{E}_A + \mathbf{E}_F \tag{3.28}$$

and

$$\mathbf{H}_{total} = \mathbf{H}_A + \mathbf{H}_F \tag{3.29}$$

Using vector potentials to construct solutions to Maxwell's equations is the subject of the next section.

3.3 Field Construction

The simplest solutions to Maxwell's equations are Transverse ElectroMagnetic (TEM) field configurations, or modes, where both the electric and magnetic field components are transverse to the direction of propagation. Modes that are Transverse Electric (TE) or Transverse Magnetic (TM) may also be constructed. The direction of propagation is indicated by superscript, i.e., TEM^z is transverse to the z direction. In this chapter, only solutions in a rectangular coordinate system are considered.

3.3.1 TEM Modes. In a source free region, both $\mathbf{J}$ and $\mathbf{M}$ do not exist. Equations (3.14) and (3.26) become the homogeneous differential equations

$$\nabla^2 \mathbf{A} + k^2 \mathbf{A} = 0 \tag{3.30}$$

and

$$\nabla^2 \mathbf{F} + k^2 \mathbf{F} = 0 \tag{3.31}$$

Since (3.30) and (3.31) are of the same form, the solutions will also be of the same form. Therefore, the following development is only be presented for $\mathbf{A}$. Letting

$$\mathbf{A}(x,y,z) = \hat{x} A_x(x,y,z) + \hat{y} A_y(x,y,z) + \hat{z} A_z(x,y,z) \tag{3.32}$$

the component form of (3.30) is

$$\nabla^2 A_x + k^2 A_x = 0 \tag{3.33a}$$

$$\nabla^2 A_y + k^2 A_y = 0 \tag{3.33b}$$

$$\nabla^2 A_z + k^2 A_z = 0 \tag{3.33c}$$

The total electric field is given by the sum of (3.15) and (3.17),

$$\mathbf{E}_{\text{total}} = \mathbf{E}_A + \mathbf{E}_F = -j\omega\mathbf{A} + \frac{1}{j\omega\epsilon\mu}\nabla(\nabla\cdot\mathbf{A}) - \frac{1}{\epsilon}\nabla\times\mathbf{F} \tag{3.34}$$

Applying (3.32) to (3.34), the total $\mathbf{E}$ field can be written in component form

$$\begin{aligned}\mathbf{E} = \hat{x}&\left[-j\omega A_x + \tfrac{1}{j\omega\epsilon\mu}\left(\tfrac{\partial^2 A_x}{\partial x^2} + \tfrac{\partial^2 A_y}{\partial x\partial y} + \tfrac{\partial^2 A_z}{\partial x\partial z}\right) - \tfrac{1}{\epsilon}\left(\tfrac{\partial F_z}{\partial y} - \tfrac{\partial F_y}{\partial z}\right)\right] \\ \hat{y}&\left[-j\omega A_y + \tfrac{1}{j\omega\epsilon\mu}\left(\tfrac{\partial^2 A_x}{\partial x\partial y} + \tfrac{\partial^2 A_y}{\partial y^2} + \tfrac{\partial^2 A_z}{\partial y\partial z}\right) - \tfrac{1}{\epsilon}\left(\tfrac{\partial F_x}{\partial z} - \tfrac{\partial F_z}{\partial x}\right)\right] \\ \hat{z}&\left[-j\omega A_z + \tfrac{1}{j\omega\epsilon\mu}\left(\tfrac{\partial^2 A_x}{\partial x\partial z} + \tfrac{\partial^2 A_y}{\partial y\partial z} + \tfrac{\partial^2 A_z}{\partial z^2}\right) - \tfrac{1}{\epsilon}\left(\tfrac{\partial F_y}{\partial x} - \tfrac{\partial F_x}{\partial y}\right)\right]\end{aligned} \tag{3.35}$$

By the Duality Principle the total magnetic field likewise is given by

$$\mathbf{H}_{\text{total}} = \mathbf{H}_A + \mathbf{H}_F = \frac{\nabla \times \mathbf{A}}{\mu} + \frac{1}{j\omega\epsilon\mu}\nabla\left(\nabla \cdot \mathbf{F}\right) - j\omega\mathbf{F} \tag{3.36}$$

which which can also be expanded in components as

$$\begin{aligned}\mathbf{H} = \hat{x}\left[-j\omega F_x + \tfrac{1}{j\omega\epsilon\mu}\left(\tfrac{\partial^2 F_x}{\partial x^2} + \tfrac{\partial^2 F_y}{\partial x \partial y} + \tfrac{\partial^2 F_z}{\partial x \partial z}\right) + \tfrac{1}{\mu}\left(\tfrac{\partial A_z}{\partial y} - \tfrac{\partial A_y}{\partial z}\right)\right] \\ \hat{y}\left[-j\omega F_y + \tfrac{1}{j\omega\epsilon\mu}\left(\tfrac{\partial^2 F_x}{\partial x \partial y} + \tfrac{\partial^2 F_y}{\partial y^2} + \tfrac{\partial^2 F_z}{\partial y \partial z}\right) + \tfrac{1}{\mu}\left(\tfrac{\partial A_x}{\partial z} - \tfrac{\partial A_z}{\partial x}\right)\right] \\ \hat{z}\left[-j\omega F_z + \tfrac{1}{j\omega\epsilon\mu}\left(\tfrac{\partial^2 F_x}{\partial x \partial z} + \tfrac{\partial^2 F_y}{\partial y \partial z} + \tfrac{\partial^2 F_z}{\partial z^2}\right) + \tfrac{1}{\mu}\left(\tfrac{\partial A_y}{\partial x} - \tfrac{\partial A_x}{\partial y}\right)\right]\end{aligned} \tag{3.37}$$

To generate a TEM^z mode, both $\mathbf{A}$ and $\mathbf{F}$ must be used as generating functions. Requiring $\mathbf{A} = \hat{z}A_z$ and $\mathbf{F} = \hat{z}F_z$ to be non-zero while $A_x = A_y = F_x = F_y = 0$ will, by (3.34) and (3.36), produce the required TEM^z field components.

3.3.2 TM,TE modes. While the use of TEM modes is sufficient for many applications (such as wave propagation in free space), other boundary conditions require the use of TM and TE modes. This nomenclature indicates that either the magnetic or electric field components lie in a plane transverse to a given direction. For example, a TE^y field configuration implies that $E_y = 0$; the remaining electric field components, and all the magnetic field components, may or may not exist.

To generate modes TM (or TE) to a given direction, it is sufficient to allow the magnetic vector potential $\mathbf{A}$ (or electric vector potential $\mathbf{F}$) to have a single non-zero component in the direction in which the fields are desired to be transverse [4]. For example, the generating potential for TM^z field components is

$$\begin{aligned}\mathbf{A} &= \hat{z}A_z\left(x, y, z\right) \\ \mathbf{F} &= 0\end{aligned} \tag{3.38}$$

where the vector potential $\mathbf{A}$ must satisfy the wave equation (3.14) with $\mathbf{J} = 0$. Using the separation of variables technique, solution is assumed to be in the form

$$A_z(x, y, z) = f(x)\, g(y)\, h(z) \tag{3.39}$$

where the functions f, g and h must be chosen to satisfy the wave equation (3.33c) and boundary conditions of the problem. For a rectangular waveguide oriented on the z-axis it is easiest to apply the boundary conditions if the solution is written in the form

$$A_z = [C_1 \cos(k_x x) + D_1 \sin(k_x x)]\,[C_2 \cos(k_y y) + D_2 \sin(k_y y)]\left(B^+ e^{-\gamma_z z} + B^- e^{\gamma_z z}\right) \tag{3.40}$$

where the complex exponentials represent traveling waves and the sine and cosine functions represent standing waves. The separation of variables also obtains the constraint equation

$$k_x^2 + k_y^2 - \gamma_z^2 = k^2 = \omega^2 \epsilon \mu \tag{3.41}$$

In (3.40), the coefficients $C, D,$ and B are amplitude constants determined upon satisfaction of the boundary conditions. The wave numbers k_x and k_y are spatial constants that describe field variation in x and y respectively, while the wavenumber k is dependent on both frequency and the fundamental properties of the medium itself. The wavenumber γ_z describes field behavior in the propagation axis, and consists of a real and imaginary part, such that $\gamma = \alpha + j\beta$. The real part α is the attenuation constant, and the imaginary part β is the phase constant.

The transverse wave numbers may also be complex, and are often referred to as eigenvalues, since they are characteristic solutions to the wave equation. The notation $e^{-\gamma_z z}$ indicates a wave traveling in the forward, $+z$, direction, while $e^{\gamma_z z}$ indicates reverse travel along $-z$. If γ_z is purely imaginary, the wave is unattenuated. If γ_z is purely real, the wave is evanescent. For complex γ_z and $Re(\gamma_z) > 0$, the wave

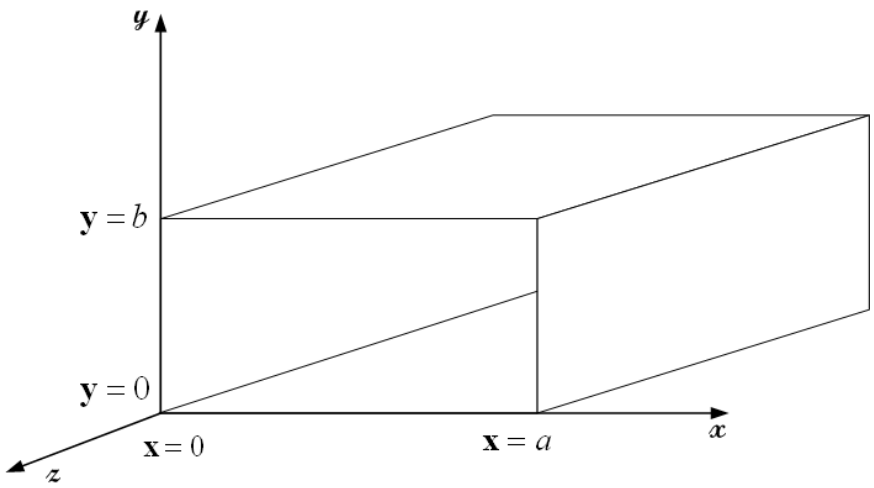

Figure 3.1: Coordinate system used thoughout this thesis. The waveguide axis is z, y is top to bottom, and x is left to right. The waveguide is filled with free space, with parameters (ϵ_0, μ_0)

.

travels within some envelope of attenuation. Once A_z is found, the **E** and **H** field components can be determined according to (3.35) and (3.37).

3.4 Guided Waves

This section presents the method for solving Maxwell's equations in a rectangular hollow waveguide with (assumed) perfect electric conducting (PEC) walls, and cross section uniform to the direction of propagation. The analysis throughout this section is similar to Chapter 8 of [16]. The geometry of the waveguide is given in Figure 3.1. Let the axis of the waveguide be the z axis, with (x, y) dimensions from the origin to (a, b); usually, $a \approx 2b$, where b is the height of the waveguide. The interior of the waveguide will be free space with electrical parameters ϵ_0 and μ_0. A TEM mode cannot propagate in a hollow waveguide due to the absence of both the axial currents and magnetic flux necessary to generate transverse field components. Therefore, solutions TM and TE will be investigated.

Transverse magnetic to z modes, as previously mentioned, are generated from $\mathbf{A} = \hat{z}A_z$ and $\mathbf{F} = 0$. Standing waves will occupy the transverse dimensions, while a

traveling wave will exist along z. Therefore, use of the magnetic vector potential in (3.40) is appropriate. Boundary conditions require that the tangential component of the electric field (E_z) vanish at $x = 0, x = a, y = 0$ and $y = b$. Therefore, f and g of (3.39) are

$$f(x) = D_1 \sin(k_x x) \quad k_x = \tfrac{m\pi}{a} \quad m = 1, 2, 3...$$
$$g(y) = D_2 \sin(k_y y) \quad k_y = \tfrac{n\pi}{b} \quad n = 1, 2, 3...$$

Each pairing of the integers m and n represent a possible mode. If only forward-traveling waves are considered, the TM^z mode functions are

$$A_z = B^+_{mn} \sin\left(\frac{m\pi x}{a}\right) \sin\left(\frac{n\pi y}{b}\right) e^{-\gamma_z z} \tag{3.42}$$

where the constants have been combined. The constraint equation (3.41) then becomes

$$\left(\frac{m\pi}{a}\right)^2 + \left(\frac{n\pi}{b}\right)^2 - \gamma_z^2 = k_0^2 = \omega^2 \epsilon_0 \mu_0 \tag{3.43}$$

The field components are obtained from (3.34) and (3.36). A solution using TE modes can be determined in a similar manner.

3.4.1 Impedance. The use of the term impedance to describe the complex ratio of voltage and current was applied, in turn, to circuit theory, transmission lines, and electromagnetic fields [24]. Several representations of impedance exist, depending on the field type, direction of travel, and the medium of propagation. The intrinsic impedance η of a material, dependent only the parameters ϵ and μ, is

$$\eta = \sqrt{\frac{\mu}{\epsilon}} \tag{3.44}$$

The wave impedance,

$$Z = \frac{E_t}{H_t} \tag{3.45}$$

is the ratio of transverse components of **E** to transverse components of **H**. The impedance is dependent on the type of wave: TEM, TE, TM all have characteris-

tic wave impedances particular to the type of waveguide, material, and frequency. If a plane wave (TEM, TE, or TM) is normally incident on the material, then the wave impedance Z is reduces to the intrinsic impedance η.

3.4.2 Cutoff Frequency. Forward wave propagation (without attenuation) in the waveguide occurs when $\gamma_z = j\beta$ is purely imaginary. When γ_z is purely real, the wave is evanescent and does not propagate. The transition between these two states occurs at the cutoff frequency, when

$$k^2 - \left(k_x^2 + k_y^2\right) = k^2 - k_c^2 = 0 \tag{3.46}$$

Since $k = \omega\sqrt{\epsilon\mu} = 2\pi f\sqrt{\epsilon\mu}$, substituting in the wavenumbers from (3.42) and solving (3.46) for frequency f results in

$$(f_c)_{mn} = \frac{1}{2\pi\sqrt{\epsilon\mu}}\sqrt{\left(\frac{m\pi}{a}\right)^2 + \left(\frac{n\pi}{b}\right)^2} \tag{3.47}$$

which is an expression for the cutoff frequency of a TM_{mn} mode. Modes (TM, TE, or both) that have the same cutoff frequency are called degenerate. The mode with the lowest cutoff frequency in a particular guide is the dominant mode. In a rectangular waveguide where $a > b$, the TE_{10}^z mode is dominant.

3.4.3 Mode Orthogonality. The solution to the PFW problem requires the use of an arbitrary number of field modes. The total field in the waveguide is the superposition of all the modes, and each mode vector $\mathbf{e}_i$ is orthogonal to all other mode vectors. If two modes, either TE or TM, are considered, multiplying them together forms the product

$$\mathbf{e_i} \cdot \mathbf{e_j} = \nabla_t \Psi_i \cdot \nabla_t \Psi_j \tag{3.48}$$

where Ψ is a mode function and ∇_t is the transverse gradient. By Green's first identity,

$$\iint \mathbf{e_i} \cdot \mathbf{e_j} ds = -\left(k_{cj}\right)^2 \iint \Psi_i \Psi_j ds \tag{3.49}$$

Also, by Green's second identity,

$$\left[\left(k_{ci}\right)^2 - \left(k_{cj}\right)^2\right] \iint \Psi_i \Psi_j ds = 0 \tag{3.50}$$

If $k_{ci} \neq k_{cj}$ the integral must vanish, as must the right hand side of (3.49), that is

$$\iint \mathbf{e_i} \cdot \mathbf{e_j} ds = 0, \quad i \neq j \tag{3.51}$$

It is equivalent to state that if the inner product of two functions (or vectors) is zero, then they are orthogonal. The proof (from Chapter 8 of [16]) may be extended to the magnetic field vectors **h** as well. The transverse electromagnetic field at any point can then be expressed as the sum of the mode vectors:

$$\mathbf{E}_t = \sum_i \mathbf{e}_i$$
$$\mathbf{H}_t = \sum_i \mathbf{h}_i$$

where the mode vectors **e** and **h** can be either TE or TM.

3.4.4 Power Transmission. When many modes in a waveguide with PEC walls exist simultaneously, each will propagate energy independently [16]. For the current test setup of a PFW this is especially relevant, since it is expected that an infinite number of TM^y modes will exist on both sides of the discontinuity. In the fully filled waveguide, all the energy is transmitted by the dominant TE_{10} mode; this allows the use of closed form algorithms, such as NRW, which consider single-mode propagation. When multiple modes exist, it is necessary to take into account the complex power transmitted by both the propagating and evanescent modes. For N modes, the total z-directed complex power in a section of waveguide is the sum of the

power contained in each mode, such that

$$\begin{aligned} P_z &= \iint (\mathbf{E} \times \mathbf{H}^*) \cdot \hat{z} ds \\ &= \iint \left(\sum_i \mathbf{e}_i V_i \right) \times \left(\sum_j \mathbf{h}_j I_j^* \right) \cdot \hat{z} ds \\ &= \sum_i \sum_j V_i I_j^* \iint \mathbf{e}_i \cdot \mathbf{e}_j ds \\ &= \sum_i V_i I_i^* \end{aligned} \tag{3.52}$$

where V_i is the mode voltage and I_i is the mode current of the ith mode. It is apparent that this is the expected result, since the complex power of any system is simply $P_z = V \cdot I^*$.

3.5 Summary

A cursory review of electromagnetics was presented in this chapter, including the use of vector potentials and the modal expansion of fields in a waveguide. These concepts form the basis of the modal analysis found in Chapter IV.

IV. Mode-Matching Analysis

The characterization of electromagnetic materials by transmission and reflection methods in a rectangular waveguide assumes the sample to be homogeneous and precisely machined, i.e. it completely fills the inner dimensions of the waveguide and is perpendicularly planar to the waveguide walls, as seen in Figure 4.1. At high temperatures, thermal expansion distorts the geometry of both the sample and the waveguide itself [21]. The metal waveguide tends to expand at a greater rate than the sample under test, resulting in air gaps between the sample and the waveguide walls. Figure 4.2 (a) is an example of a top-bottom gap in the short dimension of the waveguide. The boundary conditions at the gap require the excitation of higher order modes which are not accounted for in closed form solutions such as the NRW algorithm, which uses the dominant (TE_{10}) mode only [17, 21].

Development of the solution for a single top gap will follow that suggested by Collin [10] and Harrington [16], using TM^y modes to construct the electric and magnetic fields in the unobstructed and partially filled waveguide regions. By applying appropriate boundary conditions, and ensuring that tangential components of **E** and **H** are matched, a system of equations that accurately describes the structure can be developed. In turn, the forward reflection (S_{11}^{thy}) and transmission (S_{21}^{thy}) coefficients can be extracted. A minimization of the difference between the theoretical and experimental S-parameters is calculated according to the minimization equations

$$\begin{aligned} \left| S_{11}^{\text{thy}}(\omega, \epsilon, \mu) - S_{11}^{\text{exp}}(\omega) \right| &< tol \\ \left| S_{21}^{\text{thy}}(\omega, \epsilon, \mu) - S_{21}^{\text{exp}}(\omega) \right| &< tol \end{aligned} \tag{4.1}$$

A Newton-Raphson root search of the complex parameters ϵ and μ is performed until an acceptable minimum tolerance is reached. In addition, it is necessary to have available a reference plane independent measurement scheme to compensate for error in sample placement or if alignment with the calibration plane cannot be guaranteed. This method is presented in the final section of the chapter.

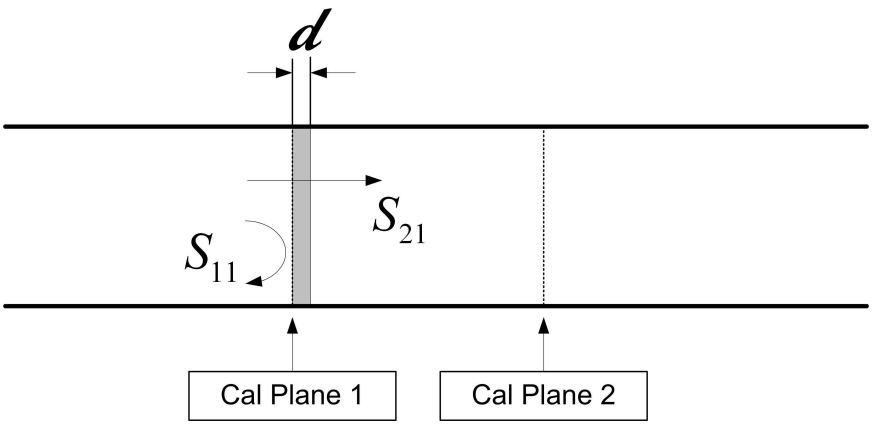

Figure 4.1: Forward scattering parameters in a fully filled waveguide measurement. The sample is aligned with calibration plane 1; calibration plane 2 is the other end of the sample holder.

4.1 Newton-Raphson Root Search

The minimization equations used in this thesis can be thought of as two functions, dependent on values of ϵ_r and μ_r that force the differences in (4.1) below the required tolerance. The complexity of the desired root search depends on the parameters of the material. If a material has both electric and magnetic loss properties, then a 2-dimensional root search, using two equations and two unknowns, must be used. However, if a material is a non-magnetic dielectric, only ϵ_r is the unknown ($\mu_r = 1$), and a complex 1-dimensional root search of one equation and one unknown can be applied. This technique will be shown first.

One of the most common techniques in numerical analysis used to determine roots of equations is the Newton-Raphson method [5]. If p is an unknown root, and a function f is differentiable on the interval of all approximations to p, then $f(p) = 0$. Let $x = x_0$ be an initial guess of the root p. A Taylor series expansion of $f(x)$ around the approximate root x_0 is

$$f(x) = f(x_0 + \Delta x) \approx f(x_0) + \Delta x f'(x_0) + \frac{\Delta x^2}{2!} f''(\xi) + ... \tag{4.2}$$

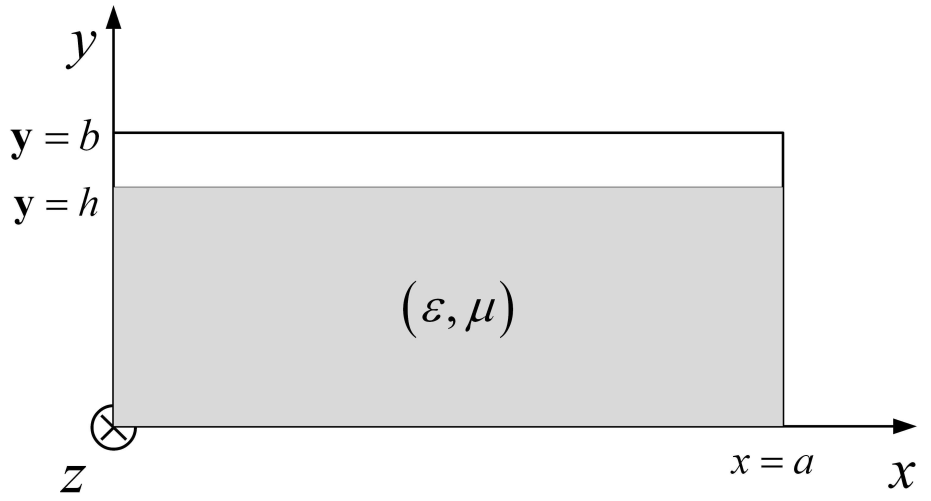

(a)

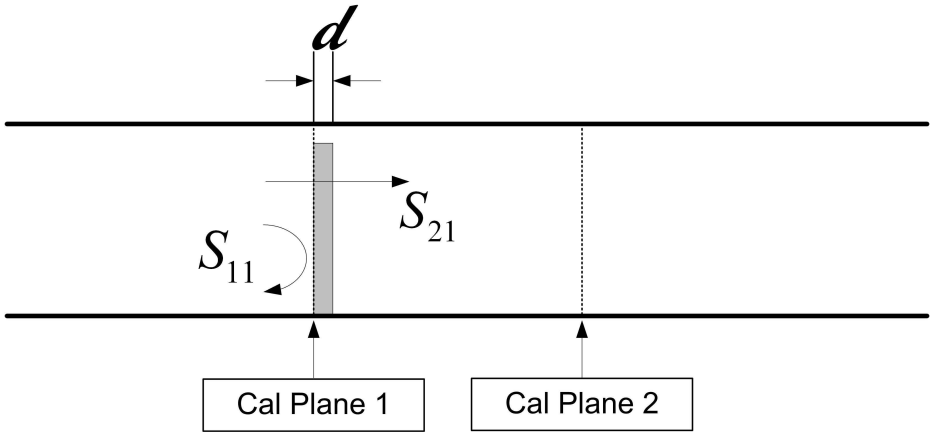

(b)

Figure 4.2: Two cross sectional views, (a) transverse and (b) axial, of a partially filled waveguide consisting of a single top air gap, with material parameters (ϵ, μ). Only the dominant mode forward scattering parameters, S_{11} and S_{21} are shown, although the PFW geometry excites infinitely many modes.

where ξ is on the range x_0 to $x_0 + \Delta x$. If the approximation $x_0 + \Delta x$ is set equal to p, then

$$f(p) = 0 \approx f(x_0) + \Delta x f'(x_0) + \frac{\Delta x^2}{2!} f''(\xi) + ... \tag{4.3}$$

he first derivative of f can be calculated numerically, using forward, central, or backward differences. If Δx is small, then the third and higher order terms can be neglected. This leads to an estimate for Δx,

$$\Delta x = -\frac{f(x_0)}{f'(x_0)} \tag{4.4}$$

The next approximation x_1 to the root is obtained by adding Δx to the previous estimate, x_0,

$$x_1 = x_0 + \Delta x = x_0 - \frac{f(x_0)}{f'(x_0)} \tag{4.5}$$

In general, then, the nth approximation to the root p is

$$x_n = x_{n-1} - \frac{f(x_{n-1})}{f'(x_{n-1})} \tag{4.6}$$

Convergence is dependent on a "good" initial guess for the root p. If the root is known to be complex, the initial guess must also be complex; the method will not converge to a complex root if a purely real initial guess is supplied [1].

If roots to more than one equation are to be found simultaneously, Newton-Raphson's method can easily be expanded to higher dimensions. Consider two functions

$$\begin{aligned} f(u, v) &= 0 \\ g(u, v) &= 0 \end{aligned} \tag{4.7}$$

with roots u and v. It is assumed both functions are differentiable on the interval, or surface, of approximations to u and v. If $x = x_0$ and $y = y_0$ are supplied as estimates

to the roots, then the Taylor series expansion around the approximations is

$$\begin{aligned} f(x,y) &= f(x_0+\Delta x, y_0+\Delta y) \approx f(x_0,y_0) + \frac{\partial f}{\partial x}\Delta x + \frac{\partial f}{\partial y}\Delta y \\ g(x,y) &= g(x_0+\Delta x, y_0+\Delta y) \approx g(x_0,y_0) + \frac{\partial g}{\partial x}\Delta x + \frac{\partial g}{\partial y}\Delta y \end{aligned} \tag{4.8}$$

where the higher order derivatives of the series have been neglected. Letting $x_0+\Delta x = u$ and $y_0 + \Delta y = v$, (4.8) reduces to

$$\begin{aligned} f(u,v) = 0 = f(x_0+\Delta x, y_0+\Delta y) &= f(x_0,y_0) + \frac{\partial f}{\partial x}\Delta x + \frac{\partial f}{\partial y}\Delta y \\ g(u,v) = 0 = g(x_0+\Delta x, y_0+\Delta y) &= g(x_0,y_0) + \frac{\partial g}{\partial x}\Delta x + \frac{\partial g}{\partial y}\Delta y \end{aligned} \tag{4.9}$$

which can be recast in matrix notation as

$$\begin{bmatrix} f_x & f_y \\ g_x & g_y \end{bmatrix} \begin{bmatrix} \Delta x \\ \Delta y \end{bmatrix} = - \begin{bmatrix} f(x_0,y_0) \\ g(x_0,y_0) \end{bmatrix} \tag{4.10}$$

The matrix can be inverted to obtain expressions for Δx and Δy,

$$\begin{bmatrix} \Delta x \\ \Delta y \end{bmatrix} = \frac{-1}{|f_x g_y - g_x f_y|} \begin{bmatrix} g_y & -f_y \\ -g_x & f_x \end{bmatrix} \begin{bmatrix} f(x_0,y_0) \\ g(x_0,y_0) \end{bmatrix} \tag{4.11}$$

Proceeding as before, the next set of estimates to the roots are found by adding Δx and Δy to the previous estimates, x_0 and y_0.

$$\begin{aligned} x_1 &= x_0 + \Delta x \\ y_1 &= y_0 + \Delta y \end{aligned} \tag{4.12}$$

The nth root approximation is therefore

$$\begin{aligned} x_n &= x_{n-1} + \Delta x_{n-1} \\ y_n &= y_{n-1} + \Delta y_{n-1} \end{aligned} \tag{4.13}$$

Depending on the slope of each function f and g, the initial guesses usually must be good approximations to the root. If the third term of the Taylor series is too large, then it may be necessary to include it in order to achieve root convergence [5].

4.2 Partially Filled Waveguide Technique

4.2.1 TM^y Modes. In rectangular waveguides where $a \approx 2b$, the dominant mode is TE_{10}; the electric field component is oriented in the $\hat{y}$ direction, and both the $\hat{x}$ and $\hat{z}$ components do not exist. Conversely, the magnetic field has non-zero components in the $\hat{x}$ and $\hat{z}$ directions, while the $\hat{y}$ component does not exist.

Recall from [16] that the components of the **E**-field of the dominant TE_{10} mode can be written as

$$\begin{aligned} e_x &= 0 \\ e_y &= E_0 \sin(k_x x)\, e^{-\gamma_z z} \\ e_z &= 0 \end{aligned}$$

and the **H**-field components as

$$\begin{aligned} h_x &= \tfrac{\gamma_z}{j\omega\mu_0} E_0 \sin(k_x x)\, e^{-\gamma_z z} \\ h_y &= 0 \\ h_z &= \tfrac{k_x}{j\omega\mu_0} E_0 \cos(k_x x)\, e^{-\gamma_z z} \end{aligned}$$

The wave impedance, by definition, is the ratio of transverse **e** and **h** vector field components of the dominant mode and is therefore equal to

$$Z_{TE^z_{10}} = \frac{e_y^{\pm}}{h_x^{\pm}} = \frac{E_0 \sin(k_x x)\, e^{\mp\gamma_z z}}{\frac{\gamma_z}{j\omega\mu_0} E_0 \sin(k_x x)\, e^{\mp\gamma_z z}} = \frac{j\omega\mu_0}{\gamma_z}. \tag{4.14}$$

Since this is equal to the wave impedance of a TM^y_{10} mode, and because all the scattered modes will be in the set of TM^y_{1n}, the complete mode set can be constructed using TM^y modes.

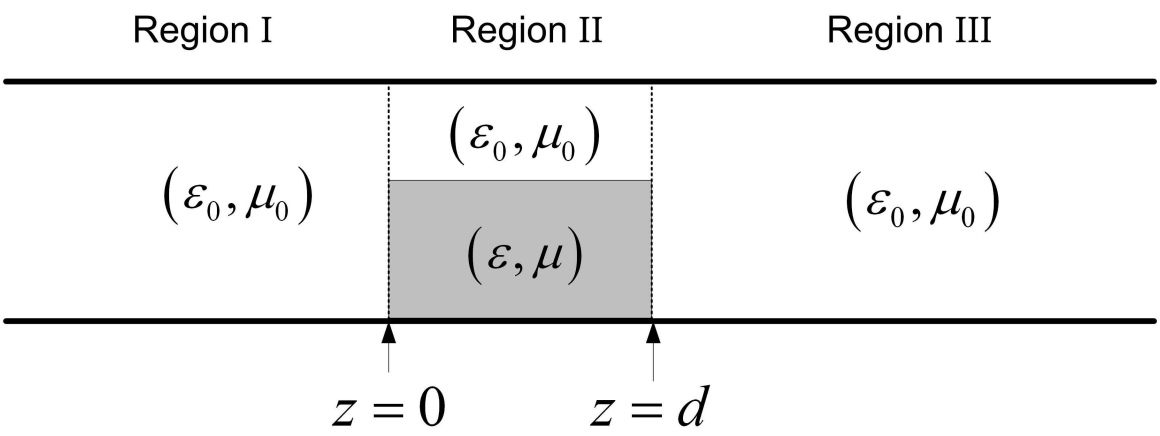

Figure 4.3: The three computational regions used in field construction: Region I: empty; Region II: PFW; Region III: empty.

4.2.2 Field Construction. It is sufficient to use the magnetic vector potential **A** to generate the necessary electromagnetic field components required for satisfying boundary conditions in all the regions of the waveguide. Figure 4.3 is a diagram of the regions discussed in this section. In the two empty regions (i.e. Regions I and III), the magnetic vector potential takes the form

$$A_y = (B_1 \sin k_x x + B_2 \cos k_x x)(C_1 \sin k_y y + C_2 \cos k_y y)\left(D^+ e^{-\gamma_0 z} + D^- e^{\gamma_0 z}\right) \quad (4.15)$$

where k_x, k_y, and γ_0 are the transverse wave numbers and complex propagation wave number, respectively, that satisfy the constraint equation in free space,

$$k_x^2 + k_y^2 - \gamma_0^2 = k_0^2 = \omega^2 \epsilon_0 \mu_0$$

The use of $e^{-\gamma_0 z}$ denotes a forward propagating wave in the $\hat{z}$ direction (i.e. through the waveguide), and γ_0 is, in general, a complex quantity. The respective **E** and **H**-fields can be generated by

$$\mathbf{E}_A = \frac{1}{j\omega\epsilon_0\mu_0}\left[\nabla(\nabla \cdot \mathbf{A}) + k_0^2 \mathbf{A}\right], \quad \mathbf{H}_A = \frac{\nabla \times \mathbf{A}}{\mu_0} \quad (4.16)$$

Substituting (4.15) into (4.16) and simplifying, the **E** components may be written as

$$\begin{aligned} e_x &= \tfrac{k_x k_y}{j\omega\epsilon_0\mu_0}\left(B_1\cos k_x x - B_2\sin k_x x\right)\left(C_1\cos k_y y - C_2\sin k_y y\right)\left(D^- e^{-\gamma_0 z} + D^- e^{\gamma_0 z}\right) \\ e_y &= \tfrac{\left(k_0^2 - k_y^2\right)}{j\omega\epsilon_0\mu_0}\left(B_1\sin k_x x + B_2\cos k_x x\right)\left(C_1\sin k_y y + C_2\cos k_y y\right)\left(D^+ e^{-\gamma_0 z} + D^- e^{\gamma_0 z}\right) \\ e_z &= \tfrac{-k_y\gamma_0}{j\omega\epsilon_0\mu_0}\left(B_1\sin k_x x + B_2\cos k_x x\right)\left(C_1\cos k_y y - C_2\sin k_y y\right)\left(D^+ e^{-\gamma_0 z} - D^- e^{\gamma_0 z}\right) \end{aligned} \tag{4.17a}$$

and the **H** components as

$$\begin{aligned} h_x &= \tfrac{\gamma_0}{\mu_0}\left(B_1\sin k_x x + B_2\cos k_x x\right)\left(C_1\sin k_y y + C_2\cos k_y y\right)\left(D^+ e^{-\gamma_0 z} - D^- e^{\gamma_0 z}\right) \\ h_y &= 0 \\ h_z &= \tfrac{k_x}{\mu_0}\left(B_1\cos k_x x - B_2\sin k_x x\right)\left(C_1\sin k_y y + C_2\cos k_y y\right)\left(D^+ e^{-\gamma_0 z} + D^- e^{\gamma_0 z}\right) \end{aligned} \tag{4.17b}$$

Satisfaction of electric field boundary conditions at the waveguide walls requires B_2 and C_1 to vanish, leading to the definition of the wave numbers k_x and k_y:

$$\begin{aligned} &k_x = \tfrac{m\pi}{a},\ k_y = \tfrac{n\pi}{b} \\ &m = 1, 2, 3, ... \\ &n = 0, 1, 2, ... \end{aligned}$$

where a is the long dimension of the waveguide cross section, and b is the short dimension, $\hat{x}$ and $\hat{y}$ respectively (refer to Figure 4.2 (a)). By the Uniqueness Theorem, it is sufficient to satisfy only the electric field condition [4].

The complex mode propagation wave number γ_0 of the empty region of the waveguide can then be written as

$$\gamma_{0_{mn}} = \sqrt{k_x^2 + k_y^2 - k_0^2} = \sqrt{\left(\frac{m\pi}{a}\right)^2 + \left(\frac{n\pi}{b}\right)^2 - k_0^2}$$

By applying the aforementioned boundary conditions, the Region I electric and magnetic field components of (4.17) can simplified as

$$\begin{aligned}
e_x &= \tfrac{-k_x k_y}{j\omega\epsilon_0\mu_0} \cos k_x x \sin k_y y \left(D^+ e^{-\gamma_0 z} + D^- e^{\gamma_0 z}\right) \\
e_y &= \tfrac{\left(k_0^2 - k_y^2\right)}{j\omega\epsilon_0\mu_0} \sin k_x x \cos k_y y \left(D^+ e^{-\gamma_0 z} + D^- e^{\gamma_0 z}\right) \\
e_z &= \tfrac{k_y \gamma_0}{j\omega\epsilon_0\mu_0} \sin k_x x \sin k_y y \left(D^+ e^{-\gamma_0 z} - D^- e^{\gamma_0 z}\right) \\
h_x &= \tfrac{\gamma_0}{\mu_0} \sin k_x x \cos k_y y \left(D^+ e^{-\gamma_0 z} - D^- e^{\gamma_0 z}\right) \\
h_y &= 0 \\
h_z &= \tfrac{k_x}{\mu_0} \cos k_x x \cos k_y y \left(D^+ e^{-\gamma_0 z} + D^- e^{\gamma_0 z}\right)
\end{aligned} \tag{4.18}$$

Using PFW theory in Region II, spatial shift factors are used to create an alternative magnetic vector potential $\mathbf{A}$, which is then applied to construct the fields in each subregion (material and free space), namely

$$\begin{aligned}
A_{y1} &= \sin k_x x \left(C_1 \sin k_{y1} y + D_1 \cos k_{y1} y\right) \left(B_n^+ e^{-\gamma_n z} + B_n^- e^{\gamma_n z}\right) \\
A_{y2} &= \sin k_x x \left(C_2 \sin k_{y2} \left(b - y\right) + D_2 \cos k_{y2} \left(b - y\right)\right) \left(C_n^+ e^{-\gamma_n z} + C_n^- e^{\gamma_n z}\right)
\end{aligned} \tag{4.19}$$

where the subscripts 1 and 2 represent each subregion.

In Region II, the electric field boundary condition in $\hat{x}$ is identical to that of Region I, namely, the tangential fields vanish at $x = 0$ and $x = a$. Therefore, a standing sine wave exists in both subregions of Region II and throughout Region I; this is manifested in the choice of harmonic functions in (4.19). From (4.16) the fields in each region can be calculated. If the sample has height h, then fields in the first

subregion $(0 < y < h)$ exist within the material:

$$
\begin{aligned}
e_{x1} &= \frac{k_x k_{y1}}{j\omega\epsilon_1\mu_1} \cos k_x x \left(C_1 \cos k_{y1} y - D_1 \sin k_{y1} y\right) \left(B_n^+ e^{-\gamma_n z} + B_n^- e^{\gamma_n z}\right) \\
e_{y1} &= \frac{\left(k_1^2 - k_{y1}^2\right)}{j\omega\epsilon_1\mu_1} \sin k_x x \left(C_1 \sin k_{y1} y + D_1 \cos k_{y1} y\right) \left(B_n^+ e^{-\gamma_n z} + B_n^- e^{\gamma_n z}\right) \\
e_{z1} &= \frac{-k_{y1}\gamma_n}{j\omega\epsilon_1\mu_1} \sin k_x x \left(C_1 \cos k_{y1} y - D_1 \sin k_{y1} y\right) \left(B_n^+ e^{-\gamma_n z} - B_n^- e^{\gamma_n z}\right) \\
h_{x1} &= \frac{\gamma_n}{\mu_1} \sin k_x x \left(C_1 \sin k_{y1} y + D_1 \cos k_{y1} y\right) \left(B_n^+ e^{-\gamma_n z} - B_n^- e^{\gamma_n z}\right) \\
h_{y1} &= 0 \\
h_{z1} &= \frac{k_x}{\mu_1} \cos k_x x \left(C_1 \sin k_{y1} y + D_1 \cos k_{y1} y\right) \left(B_n^+ e^{-\gamma_n z} + B_n^- e^{\gamma_n z}\right)
\end{aligned} \tag{4.20}
$$

Fields in the second subregion $(h < y < b)$ exist in free space:

$$
\begin{aligned}
e_{x2} &= \frac{-k_x k_{y2}}{j\omega\epsilon_0\mu_0} \cos k_x x \left(C_2 \cos k_{y2}\left(b - y\right) - D_2 \sin k_{y2}\left(b - y\right)\right) \left(C_n^+ e^{-\gamma_n z} + C_n^- e^{\gamma_n z}\right) \\
e_{y2} &= \frac{\left(k_0^2 - k_{y2}^2\right)}{j\omega\epsilon_0\mu_0} \sin k_x x \left(C_2 \sin k_{y2}\left(b - y\right) + D_2 \cos k_{y2}\left(b - y\right)\right) \left(C_n^+ e^{-\gamma_n z} + C_n^- e^{\gamma_n z}\right) \\
e_{z2} &= \frac{k_{y2}\gamma_n}{j\omega\epsilon_0\mu_0} \sin k_x x \left(C_2 \cos k_{y2}\left(b - y\right) - D_2 \sin k_{y2}\left(b - y\right)\right) \left(C_n^+ e^{-\gamma_n z} - C_n^- e^{\gamma_n z}\right) \\
h_{x2} &= \frac{\gamma_n}{\mu_0} \sin k_x x \left(C_2 \sin k_{y2}\left(b - y\right) + D_2 \cos k_{y2}\left(b - y\right)\right) \left(C_n^+ e^{-\gamma_n z} - C_n^- e^{\gamma_n z}\right) \\
h_{y2} &= 0 \\
h_{z2} &= \frac{k_x}{\mu_0} \cos k_x x \left(C_2 \sin k_{y2}\left(b - y\right) + D_2 \cos k_{y2}\left(b - y\right)\right) \left(C_n^+ e^{-\gamma_n z} + C_n^- e^{\gamma_n z}\right)
\end{aligned} \tag{4.21}
$$

Boundary conditions require that the tangential electric field must vanish at $y = 0$ and $y = b$, forcing the constants C_1 and C_2 to zero. Continuity of tangential $\mathbf{E}$ and $\mathbf{H}$ at $y = h$ requires that k_x and γ_{z_n} be the same in each subregion [16]. In addition, the tangential components $e_{x1},\ e_{x2},\ e_{z1},\ e_{z2},\ e_{x1},\ h_{x2},\ h_{z1}$ and h_{z2} must be continuous at the boundary between the subregions, $y = h$. Equating e_{z1} and e_{z2} of (4.20) and (4.21), the requirement

$$
\frac{k_{y1}\gamma_n}{j\omega\epsilon\mu} \sin\frac{\pi x}{a} \sin k_{y1} h \cdot B_n^{\pm} = \frac{-k_{y2}\gamma_n}{j\omega\epsilon_0\mu_0} \sin\frac{\pi x}{a} \sin k_{y2}(b - h) \cdot C_n^{\pm} \tag{4.22}
$$

is obtained. Similarly, the continuity between h_{z1} and h_{z2} requires

$$\frac{k_x}{\mu_1}\cos(k_x x)\cos(k_{y1}h)\cdot B_n^{\pm} = \frac{k_x}{\mu_0}\cos(k_x x)\cos k_{y2}(b-h)\cdot C_n^{\pm} \tag{4.23}$$

Using either (4.22) or (4.23), the propagation coefficient of subregion 1, $B_n^{\pm}$, can be expressed in terms of the propagation coefficient of subregion 2, $C_n^{\pm}$, that is

$$B_n^{\pm} = \frac{-k_{y2}\epsilon_1\mu_1}{k_{y1}\epsilon_0\mu_0}\frac{\sin(k_{y2}(b-h))}{\sin(k_{y1}h)}C_n^{\pm} = \frac{\mu_1}{\mu_0}\frac{\cos(k_{y2}(b-h))}{\cos(k_{y1}h)}C_n^{\pm} \tag{4.24}$$

Division of (4.22) by (4.23) gives

$$\frac{k_{y1}}{\epsilon_1}\sin k_{y1}h\cos k_{y2}(b-h) = \frac{-k_{y2}}{\epsilon_2}\sin k_{y2}(b-h)\cos k_{y1}h \tag{4.25}$$

or, equivalently

$$\frac{k_{y1}}{\epsilon_1}\sin k_{y1}h\cos k_{y2}(b-h) + \frac{k_{y2}}{\epsilon_2}\sin k_{y2}(b-h)\cos k_{y1}h = 0 \tag{4.26a}$$

$$\gamma_{z,1n}^2 = k_{y1,n}^2 + k_x^2 - k_1^2 = k_{y2,n}^2 + k_x^2 - k_0^2 \tag{4.26b}$$

such that the wave numbers in each subregion satisfy the constraint equation of (4.26b). Since both k_{y1} and k_{y2} are dependent on γ_z, (4.26a) represents a transcendental eigenvalue equation for possible values of the PFW mode-propagation constant γ_z. Therefore, the equation must be solved numerically. When the correct value of γ is found, the ratio $\frac{B_n^{\pm}}{C_n^{\pm}}$ is given by (4.24). Incorporating this ratio into (4.20), the field

components of subregion 1 are

$$
\begin{aligned}
e_{x1} &= \frac{k_x k_{y2}}{j\omega\epsilon_0\mu_0}\cos k_x x \sin k_{y1} y \frac{\sin\left(k_{y2}\left(b-h\right)\right)}{\sin\left(k_{y1}h\right)}\left(C_n^+ e^{-\gamma_n z} + C_n^- e^{\gamma_n z}\right) \\
e_{y1} &= \frac{\left(k_0^2 - k_{y2}^2\right)}{j\omega\epsilon_1\mu_0}\sin k_x x \cos k_{y1} y \frac{\cos\left(k_{y2}\left(b-h\right)\right)}{\cos\left(k_{y1}h\right)}\left(C_n^+ e^{-\gamma_n z} + C_n^- e^{\gamma_n z}\right) \\
e_{z1} &= \frac{-k_{y2}\gamma_n}{j\omega\epsilon_0\mu_0}\sin k_x \sin k_{y1} y \frac{\sin\left(k_{y2}\left(b-h\right)\right)}{\sin\left(k_{y1}h\right)}\left(C_n^+ e^{-\gamma_n z} - C_n^- e^{\gamma_n z}\right) \\
h_{x1} &= \frac{\gamma_n}{\mu_0}\sin k_x x \cos k_{y1} y \frac{\cos\left(k_{y2}\left(b-h\right)\right)}{\cos\left(k_{y1}h\right)}\left(C_n^+ e^{-\gamma_n z} - C_n^- e^{\gamma_n z}\right) \\
h_{y1} &= 0 \\
h_{z1} &= \frac{k_x}{\mu_0}\cos k_x x \frac{\cos\left(k_{y2}\left(b-h\right)\right)}{\cos\left(k_{y1}h\right)}\left(C_n^+ e^{-\gamma_n z} + C_n^- e^{\gamma_n z}\right)
\end{aligned}
\tag{4.27}
$$

and the field components of subregion 2 are

$$
\begin{aligned}
e_{x2} &= \frac{k_x k_{y2}}{j\omega\epsilon_0\mu_0}\cos k_x x \sin\left(k_{y2}\left(b-y\right)\right)\left(C_n^+ e^{-\gamma_n z} + C_n^- e^{\gamma_n z}\right) \\
e_{y2} &= \frac{\left(k_0^2 - k_{y2}^2\right)}{j\omega\epsilon_0\mu_0}\sin k_x x \cos\left(k_{y2}\left(b-y\right)\right)\left(C_n^+ e^{-\gamma_n z} + C_n^- e^{\gamma_n z}\right) \\
e_{z2} &= \frac{-k_{y2}\gamma_n}{j\omega\epsilon_0\mu_0}\sin k_x x \sin\left(k_{y2}\left(b-y\right)\right)\left(C_n^+ e^{-\gamma_n z} - C_n^- e^{\gamma_n z}\right) \\
h_{x2} &= \frac{\gamma_n}{\mu_0}\sin k_x x \cos\left(k_{y2}\left(b-y\right)\right)\left(C_n^+ e^{-\gamma_n z} - C_n^- e^{\gamma_n z}\right) \\
h_{y2} &= 0 \\
h_{z2} &= \frac{k_x}{\mu_0}\cos k_x x \cos\left(k_{y2}\left(b-y\right)\right)\left(C_n^+ e^{-\gamma_n z} + C_n^- e^{\gamma_n z}\right)
\end{aligned}
\tag{4.28}
$$

The wave number γ_z is determined using the height iteration method discussed in Section 4.2.6. The wave numbers k_{y1} and k_{y2}, which represent variation in the $\hat{y}$ direction in each subregion, are not expected to be equal to each other. The fields in each of the three regions having now been constructed, it becomes possible to define the system modes.

4.2.3 Modal Analysis. In an empty waveguide, only the dominant mode propagates completely through the waveguide. All other higher-order modes are

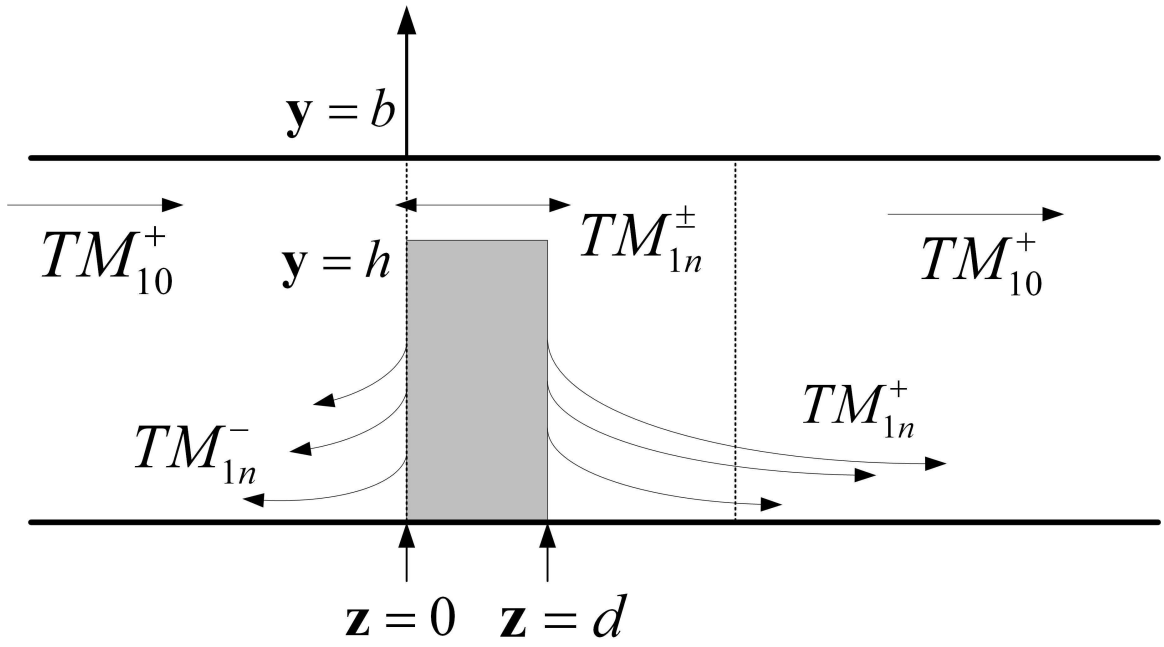

Figure 4.4: The TM^y_{10} mode is incident on the sample, and scatters the mode set $\mathrm{TM}^{\pm y}_{1n}$. Hybrid TM^y modes exist in Region II, between $z = 0$ and $z = d$. In Region III ($z > d$), forward propagating TM^y modes exist. All modes for $n > 0$ are evanescent.

evanescent and rapidly decay before reaching the network analyzer ports. For the geometry described, which is discontinuous in $\hat{y}$, the dominant mode is TM^y_{10} and the scattered mode set is TM^y_{1n}, where the index n indicates the mode number. Figure 4.4 shows a cross section of the waveguide, and illustrates the decay of the evanescent modes below cutoff as well as the propagation of the dominant mode.

In any region of the system, the total transverse electric and magnetic field can be represented as the superposition of the forward and reverse propagating modes:

$$\begin{aligned} \mathbf{E}_t &= \sum_{n=1}^{\infty} a_n^{\pm} \mathbf{e}_n e^{\mp \gamma_n z} \\ \mathbf{H}_t &= \sum_{n=1}^{\infty} \pm a_n^{\pm} \mathbf{h}_n e^{\mp \gamma_n z} \end{aligned} \tag{4.29}$$

where the coefficients $a_n^{\pm}$ represent the complex weighting constants of each mode. The field vectors $\mathbf{e}_n$ and $\mathbf{h}_n$ describe the vector components of the electric and magnetic fields of each mode, respectively [13]. Depending on the value of z, either the complex

propagation wave number of free space γ_0, or that of the PFW region, γ_z should be used.

Using (4.29) as a guide, the total transverse fields in each region of the system can be constructed. In Region I ($z < 0$), a TM_{10}^{y} mode propagates in the forward direction, and an infinite number of TM_{1n}^{y} modes scatter in the reverse direction due to scattering from the sample (see Figure 4.4). Now (4.29) can be expressed as

$$\begin{aligned}
\mathbf{E} &= a_{10}^{+}\mathbf{e}_{10}e^{-\gamma_{0,10}z} + \sum_{n=0}^{\infty} a_{1n}^{-}\mathbf{e}_{1n}e^{\gamma_{0,1n}z} \\
\mathbf{H} &= a_{10}^{+}\mathbf{h}_{10}e^{-\gamma_{0,10}z} - \sum_{n=0}^{\infty} a_{1n}^{-}\mathbf{h}_{1n}e^{\gamma_{0,1n}z} \\
\gamma_{0,1n}^{2} &= \left(\tfrac{\pi}{a}\right)^{2} + \left(\tfrac{n\pi}{b}\right)^{2} - k_0^{2}
\end{aligned} \tag{4.30}$$

Although an infinite number of reverse scattered modes exist, only the $n = 0$ mode will propagate completely through the waveguide to the network analyzer.

In Region II ($0 < z < d$), the existence of an infinite number of forward and reverse traveling modes are necessary to satisfy the boundary conditions at the discontinuity in the geometry of the sample. The transverse fields can be written as

$$\begin{aligned}
\mathbf{E} &= \sum_{n=0}^{\infty} b_{1n}^{+}\tilde{\mathbf{e}}_{1n}e^{-\gamma_{1n}z} + \sum_{n=0}^{\infty} b_{1n}^{-}\tilde{\mathbf{e}}_{1n}e^{\gamma_{1n}z} \\
\mathbf{H} &= \sum_{n=0}^{\infty} b_{1n}^{+}\tilde{\mathbf{h}}_{1n}e^{-\gamma_{1n}z} - \sum_{n=0}^{\infty} b_{1n}^{-}\tilde{\mathbf{h}}_{1n}e^{\gamma_{1n}z}
\end{aligned} \tag{4.31}$$

The use of the tilde ($\sim$) for the Region II field vectors indicates their dependence on position in y. A different vector potential is used to generate the fields of each subregion. The propagation of modes in Region II depends on several factors, including the size of the gap and the nature of the material under test. The size of the gap dictates whether a mode is propagating or evanescent. If the material sample is lossy, no true cutoff exists and all modes will propagate, although the modes that exist above the operation frequency will rapidly decay [17].

In Region III ($z > d$), the total fields can be represented by the forward propagating mode set of TM_{1n}^{y}; no reverse traveling waves are present due to the absence

of reflecting obstacles in this region. The final mode set can be described by

$$\begin{aligned}\mathbf{E} &= \sum_{n=0}^{\infty} c_{1n}^{+}\mathbf{e}_{1n}e^{-\gamma_{0,1n}(z-d)} \\ \mathbf{H} &= \sum_{n=0}^{\infty} c_{1n}^{+}\mathbf{h}_{1n}e^{-\gamma_{0,1n}(z-d)}\end{aligned} \tag{4.32}$$

where γ_0 is the propagation wave number of free space. A phase shift has been introduced into the complex exponential to facilitate matching of boundary conditions between regions.

4.2.4 Boundary Conditions. It is necessary to maintain continuity of the transverse $\mathbf{E}$ and $\mathbf{H}$ field components at the interfaces between each region, namely at $z = 0$ and $z = d$, which implies the satisfaction of the conditions

$$\begin{aligned}e_y^I\left(z=0^-\right) &= e_y^{II}\left(z=0^+\right) \\ e_x^I\left(z=0^-\right) &= e_x^{II}\left(z=0^+\right) \\ h_x^I\left(z=0^-\right) &= h_x^{II}\left(z=0^-\right) \\ e_y^{II}\left(z=d^-\right) &= e_y^{III}\left(z=d^+\right) \\ e_x^{II}\left(z=d^-\right) &= e_x^{III}\left(z=d^+\right) \\ h_x^{II}\left(z=d^-\right) &= h_x^{III}\left(z=d^+\right)\end{aligned} \tag{4.33}$$

Since the scattered mode set is TM^y, the field components h_y do not exist. It will be shown that this allows e_x to be written as a function of the field components e_y and h_x, thereby eliminating the need to satisfy e_x explicitly.

From (3.1) and (3.2), Maxwell's curl equations (Faraday's Law and Ampere's Law) in a source free region are

$$\nabla \times \mathbf{E} = -j\omega\mu\mathbf{H}$$

$$\nabla \times \mathbf{H} = j\omega\epsilon\mathbf{E}$$

Performing the curl in rectangular coordinates, and letting $h_y = 0$, this can be expanded into six equations,

$$\frac{\partial e_z}{\partial y} - \frac{\partial e_y}{\partial z} = -j\omega\mu h_x \tag{4.34a}$$

$$\frac{\partial e_x}{\partial z} - \frac{\partial e_z}{\partial x} = 0 \tag{4.34b}$$

$$\frac{\partial e_y}{\partial x} - \frac{\partial e_x}{\partial y} = -j\omega\mu h_z \tag{4.34c}$$

$$\frac{\partial h_z}{\partial y} = j\omega\epsilon e_x \tag{4.34d}$$

$$\frac{\partial h_x}{\partial z} - \frac{\partial h_z}{\partial x} = j\omega\epsilon e_y \tag{4.34e}$$

$$-\frac{\partial h_x}{\partial y} = j\omega\epsilon e_z \tag{4.34f}$$

Performing the partial derivative on e_x in (4.34b) and using the expression for e_x from (4.17) yields

$$\mp\gamma_z e_x = \frac{\partial e_z}{\partial x} \tag{4.35}$$

where the sign is chosen with respect to either forward or reverse traveling waves. It will be carried through the development. This result is combined with (4.34d) to obtain the equality

$$e_x = \frac{1}{\mp\gamma_z}\frac{\partial e_z}{\partial x} = \frac{1}{j\omega\epsilon}\frac{\partial h_z}{\partial y} \tag{4.36}$$

From (4.34c), the expression for h_z is

$$\begin{aligned} h_z &= \frac{1}{-j\omega\mu}\left(\frac{\partial e_y}{\partial x} - \frac{\partial e_x}{\partial y}\right) \\ &= \frac{1}{j\omega\mu}\left(\frac{\partial e_x}{\partial y} - \frac{\partial e_y}{\partial x}\right) \end{aligned} \tag{4.37}$$

and from (4.34f), the expression for e_z is

$$e_z = -\frac{1}{j\omega\epsilon}\frac{\partial h_x}{\partial y} \tag{4.38}$$

Substituting (4.37) and (4.38) into (4.36) and distributing the derivative operator obtains

$$\begin{aligned} e_x &= \frac{1}{\mp\gamma_z}\frac{\partial}{\partial x}\left(-\frac{1}{j\omega\epsilon}\frac{\partial h_x}{\partial y}\right) = \frac{1}{j\omega\epsilon}\frac{\partial}{\partial y}\left[\frac{1}{j\omega\mu}\left(\frac{\partial e_x}{\partial y}-\frac{\partial e_y}{\partial x}\right)\right] \\ &= \frac{\pm 1}{j\omega\epsilon\gamma_z}\frac{\partial^2 h_x}{\partial x\partial y} = -\frac{1}{\omega^2\epsilon\mu}\left(\frac{\partial^2 e_x}{\partial y^2}-\frac{\partial^2 e_y}{\partial y\partial x}\right) \end{aligned} \tag{4.39}$$

Taking the two terms on the right hand side of (4.39), substituting $\frac{\partial^2 e_x}{\partial y^2} = -k_y^2 e_x$, multiplying both sides by $\omega^2\epsilon\mu$, and rearranging terms yields

$$e_x = \frac{1}{k_y^2}\left(\frac{\pm j\omega\mu}{\gamma_z}\frac{\partial^2 h_x}{\partial x\partial y}-\frac{\partial^2 e_y}{\partial y\partial x}\right) \tag{4.40}$$

The total transverse field consists of both forward and reverse propagating modes, and the $(\pm)$ is applied to each type of mode respectively. At material boundaries, regardless of the presence of discontinuities, tangential **E** and **H** and their derivatives must be continuous [10,16]. Having shown that e_x is linearly dependent on the second derivatives of e_y and h_x, the interfacial boundary conditions on e_y and h_x will be satisfied analytically. The resultant continuity of e_x can be shown numerically given a successful solution of the mode matching matrix of (4.56).

Region II is divided into two subregions, each with different material parameters. Therefore, continuity of e_y and h_x, and also (4.40), must satisfy the boundary conditions (4.33) piecewise, that is

$$e_y^I\big|_{z=0^-} = \left\{ \begin{array}{l} e_{y1}^{II}, 0<y<h \\ e_{y2}^{II}, h<y<b \end{array} \right|_{z=0^+} \tag{4.41}$$

$$e_x^I\big|_{z=0^-} = \left\{ \begin{array}{l} e_{x1}^{II}, 0<y<h \\ e_{x2}^{II}, h<y<b \end{array} \right|_{z=0^+} \tag{4.42}$$

$$h_x^I\big|_{z=0^-} = \left\{ \begin{array}{l} h_{x1}^{II}, 0 < y < h \\ h_{x2}^{II}, h < y < b \end{array} \right|_{z=0^+} \tag{4.43}$$

at the $z = 0$ plane. Additionally, at the $z = d$ plane, the piecewise equalities

$$\left.\begin{array}{l} e_{y1}^{II}, 0 < y < h \\ e_{y2}^{II}, h < y < b \end{array}\right\}\Bigg|_{z=d^-} = e_y^{III}\big|_{z=d^+} \tag{4.44}$$

$$\left.\begin{array}{l} e_{x1}^{II}, 0 < y < h \\ e_{x2}^{II}, h < y < b \end{array}\right\}\Bigg|_{z=d^-} = e_x^{III}\big|_{z=d^+} \tag{4.45}$$

$$\left.\begin{array}{l} h_{x1}^{II}, 0 < y < h \\ h_{x2}^{II}, h < y < b \end{array}\right\}\Bigg|_{z=d^-} = h_x^{III}\big|_{z=d^+} \tag{4.46}$$

must hold, where e_x^{II}, e_y^{II} and h_x^{II} are functions of position in y, corresponding to the vector field components of each respective subregion. The total fields are matched at the boundary are the superposition of an infinite number of higher order modes, which must be truncated through practically to N modes for computational purposes.

Now that the required transverse field components, namely e_y and h_x, have been identified, the boundary conditions of (4.33) can be applied to the mode sets of (4.30), (4.31), and (4.32). The superposition of N modes yields the transverse fields

$$\begin{aligned} \mathbf{e}_{10} + \sum_{n=0}^{N-1} \Gamma_n \mathbf{e}_{1n} &= \sum_{n=0}^{N-1} t_n \tilde{\mathbf{e}}_{1n} + \sum_{n=0}^{N-1} r_n \tilde{\mathbf{e}}_{1n} \\ \mathbf{h}_{10} - \sum_{n=0}^{N-1} \Gamma_n \mathbf{h}_{1n} &= \sum_{n=0}^{N-1} t_n \tilde{\mathbf{h}}_{1n} - \sum_{n=0}^{N-1} r_n \tilde{\mathbf{h}}_n \\ \sum_{n=0}^{N-1} t_n \tilde{\mathbf{e}}_{1n} e^{-\gamma_{1n} d} + \sum_{n=0}^{N-1} r_n \tilde{\mathbf{e}}_{1n} e^{\gamma_{1n} d} &= \sum_{n=0}^{N-1} T_n \mathbf{e}_{1n} \\ \sum_{n=0}^{N-1} t_n \tilde{\mathbf{h}}_{1n} e^{-\gamma_{1n} d} - \sum_{n=0}^{N-1} r_n \tilde{\mathbf{h}}_{1n} e^{\gamma_{1n} d} &= \sum_{n=0}^{N-1} T_n \mathbf{h}_{1n} \end{aligned} \tag{4.47}$$

where the leading coefficients have been normalized with respect to a_{10}^{+}, resulting in

$$\Gamma_n = \frac{a_{1n}^{-}}{a_{10}^{+}}, \quad r_n = \frac{b_{1n}^{-}}{a_{10}^{+}}, \quad t_n = \frac{b_{1n}^{+}}{a_{10}^{+}}, \quad T_n = \frac{c_{1n}^{+}}{a_{10}^{+}} \tag{4.48}$$

The constants of (4.48) correspond to the interfacial reflection and transmission coefficients of the sample, at the front (Γ_n, t_n) and back (r_n, T_n) sample interfaces, respectively. The required S-parameters of the system can be determined from the mode coefficients, as they are simply

$$\begin{aligned} S_{11}^{\text{thy}} &= \Gamma_1 = \tfrac{a_1^{-}}{a_1^{+}} \\ S_{21}^{\text{thy}} &= T_1 = \tfrac{c_1^{+}}{a_1^{+}} \end{aligned} \tag{4.49}$$

If the sample is a simple material, the reverse S-parameters can be accurately equated to the forward parameters, that is

$$\begin{aligned} S_{22}^{\text{thy}} &= S_{11}^{\text{thy}} \\ S_{12}^{\text{thy}} &= S_{21}^{\text{thy}} \end{aligned} \tag{4.50}$$

4.2.5 Making a Well-Posed Problem. The system of (4.47) contains 4 equations and $4N$ unknowns and is therefore underdetermined for $n > 1$. If the problem is to be well-posed, an equal number of equations and unknowns must exist. Since the number of unknowns cannot be reduced, a method to construct $4N$ equations must be used. Physically, this matrix represents the coupling of modes between regions of empty waveguide and partially filled waveguide. While only the dominant mode $(n = 0)$ will propagate through the entire guide, complex power will also be transmitted and/or stored by the higher-order modes $(n > 0)$ which must be accounted for if an accurate model of the fields is to be proposed.

The satisfaction of the boundary conditions between regions presented in Section 4.2.4 required equating a single vector component of both the transverse electric and magnetic fields, that is the e_y and h_x components. A suitable testing operator should

reduce system complexity without altering the resultant S-parameters. To ease the required computations, mutually orthogonal operators are desirable. Inspection of (4.17), (4.20) and (4.21) shows that the $\sin(k_x x)$ term is common to the required vectors. The argument of the cosine term, however, is different in each region. Since it is known that in Region I, $k_y = \frac{n\pi}{b}$, an appropriate testing operator is

$$\psi = \cos\left(\frac{p\pi y}{b}\right), \quad p = 0, 1, 2, ...N \tag{4.51}$$

to be applied to each mode vector,

$$\langle \psi, f \rangle = \int \psi \cdot f dy \tag{4.52}$$

which is the inner product of a mode vector f and the testing function ψ. This choice of operation, when used on the fields of Regions I and III, will cause many terms to vanish, since sinusoidal functions of different mode indices are mutually orthogonal. The linear dependence of e_x on the field components e_y and h_x removes the requirement to integrate the testing function over the waveguide cross section, as is often done in other methods [7,13,17,18]. The testing operation is applied term by term to the linear system of equations in (4.47), which can then be written as

$$\begin{aligned}
\sum_{n=0}^{N-1} \Gamma_n \langle \mathbf{e}_{1n}, \psi \rangle - \sum_{n=0}^{N-1} r_n \langle \tilde{\mathbf{e}}_{1n}, \psi \rangle - \sum_{n=0}^{N-1} t_n \langle \tilde{\mathbf{e}}_{1n}, \psi \rangle + 0 &= \langle -\mathbf{e}_{10}, \psi \rangle \\
\sum_{n=0}^{N-1} \Gamma_n \langle \mathbf{h}_{1n}, \psi \rangle - \sum_{n=0}^{N-1} r_n \left\langle \tilde{\mathbf{h}}_{1n}, \psi \right\rangle + \sum_{n=0}^{N-1} t_n \left\langle \tilde{\mathbf{h}}_{1n}, \psi \right\rangle, +0 &= \langle \mathbf{h}_{10}, \psi \rangle \\
0 + \sum_{n=0}^{N} r_n \langle \tilde{\mathbf{e}}_{1n}, \psi \rangle e^{\gamma_{1n} d} + \sum_{n=0}^{N-1} t_n \langle \tilde{\mathbf{e}}_{1n}, \psi \rangle e^{-\gamma_{1n} d} - \sum_{n=0}^{N-1} T_n \langle \mathbf{e}_{1n}, \psi \rangle &= 0 \\
0 + \sum_{n=0}^{N} r_n \left\langle \tilde{\mathbf{h}}_{1n}, \psi \right\rangle e^{\gamma_{1n} d} - \sum_{n=0}^{N-1} t_n \left\langle \tilde{\mathbf{h}}_{1n}, \psi \right\rangle e^{-\gamma_{1n} d} + \sum_{n=0}^{N-1} T_n \langle \mathbf{h}_{1n}, \psi \rangle &= 0
\end{aligned} \tag{4.53}$$

To further reduce the required number of calculations, it is useful to observe that the transverse $\mathbf{e}$ and $\mathbf{h}$ field components have similar spatial variation, containing

harmonic functions of identical arguments. This means that the testing operation integrals need only be calculated once, and then can be multiplied by an appropriate scaling factor to correspond to the necessary field component. To facilitate anticipated matrix algebra, the testing operations of (4.53) corresponding to the electric field mode vectors can be represented by submatrices, such that

$$\begin{aligned} M_{np} &= \langle \mathbf{e}_{1n}, \psi \rangle \\ N_{np} &= \zeta \cdot U_{np} + V_{np} \\ U_{np} &= \langle \tilde{\mathbf{e}}_1, \psi \rangle \\ V_{np} &= \langle \tilde{\mathbf{e}}_2, \psi \rangle \end{aligned} \tag{4.54}$$

where ζ is the scaling factor from (4.24). Submatrices U_{np} and V_{np} correspond to the testing operation applied to the electric field vector of subregions 1 and 2, respectively. When the inner product is performed on the magnetic field vectors, the resultant submatrices are

$$\begin{aligned} P_{np} &= \tfrac{1}{Z} \langle \mathbf{e}_{1n}, \psi \rangle \\ Q_{np} &= \zeta \cdot F_{np} + G_{np} \\ F_{np} &= \tfrac{1}{Z_1} \langle \tilde{\mathbf{e}}_1, \psi \rangle \\ G_{np} &= \tfrac{1}{Z_2} \langle \tilde{\mathbf{e}}_2, \psi \rangle \end{aligned} \tag{4.55}$$

where Z is the z-directed wave impedance in each region, and the notation is that of (4.54). The respective integrals of (4.54) and (4.55) are presented in Appendix B

Using (4.54) and (4.55), the system of (4.53) can be represented in matrix form as

$$\begin{bmatrix} M_{np} & -N_{np} & -N_{np} & 0 \\ -P_{np} & Q_{np} & -Q_{np} & 0 \\ 0 & e^{-\gamma_{1n}t}N_{np} & e^{\gamma_{1n}t}N_{np} & -M_{np} \\ 0 & e^{-\gamma_{1n}t}Q_{np} & -e^{\gamma_{1n}t}Q_{np} & -P_{np} \end{bmatrix} \begin{bmatrix} \Gamma_n \\ r_n \\ t_n \\ T_n \end{bmatrix} = \begin{bmatrix} -M_{0p} \\ -P_{0p} \\ 0 \\ 0 \end{bmatrix} \tag{4.56}$$

The system is now in the form $\mathbf{Ax} = \mathbf{B}$, where each submatrix of $\mathbf{A}$ is of dimension $N \times N$, making the entire matrix $4N \times 4N$. Both the solution set $\mathbf{x}$ and the excitation vector $\mathbf{B}$ are $4N \times 1$ column vectors.

In order to numerically verify the continuity of the e_x fields across the interfacial boundary, the coefficients of the solution set $\mathbf{x}$ are used to check the boundary conditions on e_x,

$$\begin{gathered}\sum_{n=0}^{N-1}\Gamma_n e_{x,1n}-\left(\sum_{n=0}^{N-1}t_n\tilde{e}_{x,1n}+\sum_{n=0}^{N-1}r_n\tilde{e}_{x,1n}\right)=0\\ \left(\sum_{n=0}^{N-1}t_n\tilde{e}_{x,1n}e^{-\gamma_z d}+\sum_{n=0}^{N-1}r_n\tilde{e}_{x,1n}e^{\gamma_z d}\right)-\sum_{n=0}^{N-1}T_n e_{x,1n}=0\end{gathered}\tag{4.57}$$

This was calculated with several combinations of height h and total modes N, with absolute differences on the order of 10^{-15}. Together with (4.40), this verifies that the fields are continuous across the regional boundaries.

As has already been indicated, the S-parameters S_{11}^{thy} and S_{21}^{thy} are identically Γ_1 and T_1 of the solution set. The minimization equation (4.1) can now be used to search for the correct values of ϵ and μ.

4.2.6 Height Iteration Method. It has been stated that the eigenvalue equation of (4.26a) is a transcendental equation for possible values of the complex propagation wave number $\gamma_{z,PFW}$ and must be solved numerically [1]. A good initial guess is imperative to successfully finding the root of the equation. The value of $\gamma_{z,FFW}$ of the fully fillwed waveguide (FFW) is used as the initial, unperturbed guess for $\gamma_{z,PFW}$ in (4.26a) with an initial guess as $h = b - \delta$, where δ is a small value.

A Newton-Raphson root search algorithm, using central-difference derivatives, uses these values to converge on a new γ, which becomes the initial guess in the next iteration. The height h is decreased again by δ, and the process repeats until the input height h is the actual value. If the final iteration converges, then γ is accepted as γ_{PFW}, which is used to fill the mode matrix of (4.56). The top-level root search, using the minimization equation of (4.1), continues the iteration for parameters ϵ and μ.

4.3 Reference Plane Independent Measurement

The two measurements discussed in the previous section, S_{11} and S_{21}, are the reflection and transmission S-parameters, respectively. The reflection measurement is highly dependent on the sample location relative to the calibration plane along the z-axis (see Figure 4.1), since a change in position incurs a two-way phase delay (or advance) in the measurement. The transmission measurement is not sensitive to the placement of the sample.

To perform calculations, it is necessary to extract the true S-parameters (denoted with superscript ^{s}) from the measured S-parameters (denoted with superscript ^{ms}) obtained from the network analyzer. This section will assume that the sample has thickness d, and is in a waveguide sample holder of width w. Also, the notation k_z, instead of γ_z, is used for the propagation wave number. Using Figure 4.5 (a) as a guide, and using complex exponential notation to denote phase shifts, the measured S-parameters are:

$$\begin{aligned} S_{11}^{ms} &= S_{11}^{s} \\ S_{22}^{ms} &= e^{-jk(w-d)} S_{22}^{s} e^{-jk(w-d)} = e^{-jk2(w-d)} S_{22}^{s} \\ S_{21}^{ms} &= e^{-jk(w-d)} S_{21}^{s} \\ S_{12}^{ms} &= e^{-jk(w-d)} S_{12}^{s} \end{aligned} \tag{4.58}$$

Upon de-embedding the S-parameters, the actual material S-parameters are found to be

$$\begin{aligned} S_{11}^{s} &= S_{11}^{ms} \\ S_{22}^{s} &= e^{jk2(w-d)} S_{22}^{ms} \\ S_{21}^{s} &= e^{jk(w-d)} S_{21}^{ms} \\ S_{12}^{s} &= e^{jk(w-d)} S_{12}^{ms} \end{aligned} \tag{4.59}$$

The preceding equations presume that the sample is precisely aligned with the calibration plane. If, however, the alignment is erroneous, or if the sample shifts during actual measurements, the extraction of parameters in (4.59) is invalid. Consider the

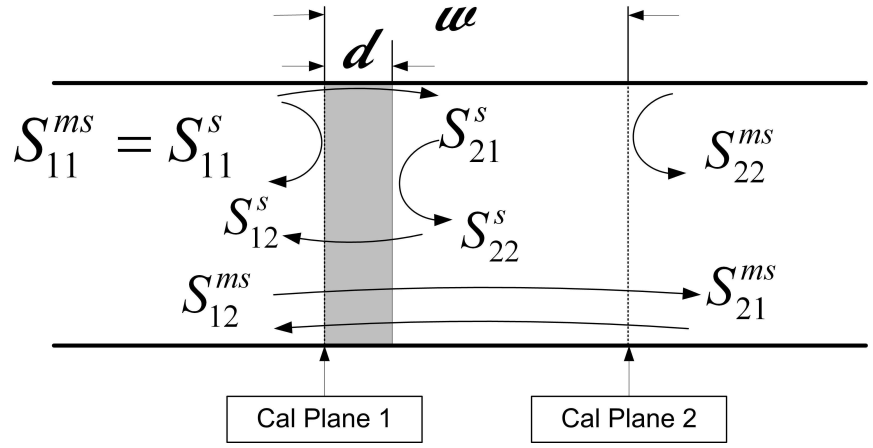

(a)

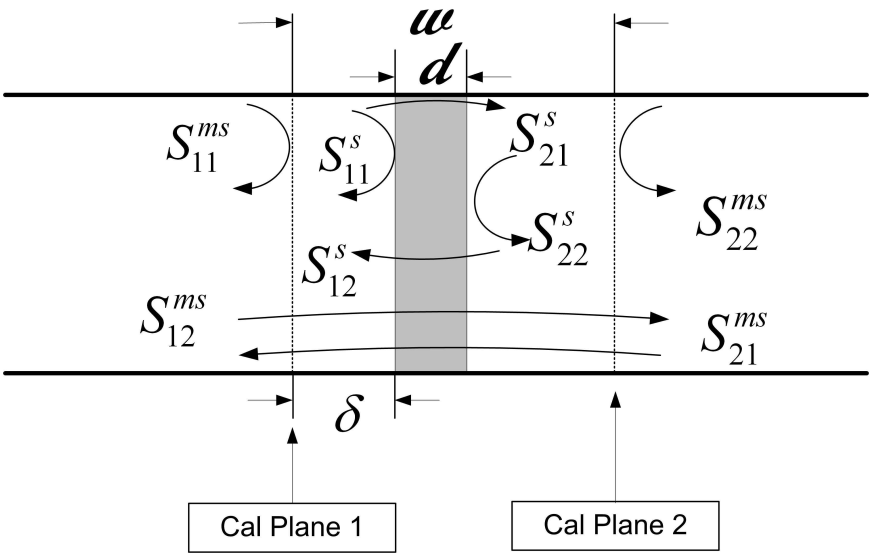

(b)

Figure 4.5: Diagram of a waveguide sample undergoing a longitudinal position shift. (a) Sample (^{s}) and measured (^{ms}) S-parameters of a sample. The sample is aligned with Calibration Plane 1. (b) The sample has been shifted δ along the axis, and $\delta \ll d$. The two reflection measurements now contain an additional phase shift of $e^{\pm jk2\delta}$.

situation of Figure 4.5 (b) when the sample is shifted along the waveguide a small distance $\delta \ll d$. The actual S-parameters are then

$$\begin{aligned} S_{11}^s &= e^{jk2\delta} S_{11}^{ms} \\ S_{22}^s &= e^{jk2(w-d-\delta)} S_{22}^{ms} \\ S_{21}^s &= e^{jk(w-d)} S_{21}^{ms} \\ S_{12}^s &= e^{jk(w-d)} S_{12}^{ms} \end{aligned} \tag{4.60}$$

It can be seen that the forward and reverse transmission measurements of (4.60) and (4.59) are the same. However, the forward and reverse reflection measurements of (4.60) incorporate the two-way phase delay/advance caused by the shift. Even a small value of δ will cause a significant phase shift of the S-parameters.

It is quite possible that, in the course of handling the material sample and the waveguide system, the exact distance between the sample and the calibration plane may not be known. During high-temperature measurements, this problem can be exacerbated by waveguide expansion in extreme heat. To perform accurate material characterization in these situations, it is necessary to eliminate the dependence on the reference plane. By multiplying the forward and reverse reflection measurements

$$\begin{aligned} S_{11}^s S_{22}^s &= \left(e^{jk2\delta} S_{11}^{ms}\right)\left(e^{jk2(w-d-\delta)} S_{22}^{ms}\right) \\ &= e^{jk2(w-d)} S_{11}^{ms} S_{22}^{ms} \end{aligned} \tag{4.61}$$

and the forward and reverse transmission measurements

$$\begin{aligned} S_{21}^s S_{12}^s &= \left(e^{jk(w-d)} S_{21}^{ms}\right)\left(e^{jk(w-d)} S_{12}^{ms}\right) \\ &= e^{j2k(w-d)} S_{21}^{ms} S_{12}^{ms} \end{aligned} \tag{4.62}$$

the dependence on δ drops out. The remaining quantities (w,d, and k_z) are all known values. When using a root search method to determine permittivity and permeability,

these products can be used in a system of minimization equations

$$\begin{aligned} \left| S_{11}^{\text{thy}} S_{22}^{\text{thy}} - S_{11}^{\text{exp}} S_{22}^{\text{exp}} \right| &< tol \\ \left| S_{21}^{\text{thy}} S_{12}^{\text{thy}} - S_{21}^{\text{exp}} S_{12}^{\text{exp}} \right| &< tol \end{aligned} \tag{4.63}$$

In a simple material, the respective forward and reverse reflection and transmission measurements are equal, i.e. $S_{11} = S_{22}$ and $S_{21} = S_{12}$. This allows Γ_1 and T_1 of the solution set of (4.56) to be used for both the forward and reverse coefficients, saving significant computational effort.

4.4 Summary

A method for characterizing an electromagnetic material that partially fills a rectangular metal waveguide in one dimension was presented using TM^y modal analysis. The matrix $\mathbf{A}$ contains the region-to-region mode coupling information and the solution vector $\mathbf{x}$ relates $\mathbf{A}$ to the field excitation vector $\mathbf{B}$. The theoretical reflection and transmission coefficients of the dominant mode, S_{11}^{thy} and S_{21}^{thy}, are extracted from $\mathbf{x}$ and compared to the experimental S-parameters. A 2-D Newton-Raphson root search iterates the parameters ϵ_r and μ_r until the absolute difference between the theoretical data and experimental data is within a specified tolerance.

In addition, a method was developed for removing measurement dependence on a sample's axial position in the waveguide with respect to the reference plane. This was accomplished by multiplying the forward and reverse reflection measurements $\left(S_{11}^{\text{thy}} \text{ and } S_{22}^{\text{thy}}\right)$ and the forward and reverse transmission measurements $\left(S_{21}^{\text{thy}} \text{ and } S_{21}^{\text{thy}}\right)$, which are then compared to the products of the respective experimental S-parameters. A 2-D Newton-Raphson root search is again used to arrive at a usable solution.

V. Results

The PFW measurement correction and the reference plane independence analysis were developed in the previous chapter for the case of a single air gap between the top of the material sample and the waveguide. The analysis uses mode matching to calculate the full set of theoretical scattering parameters and compares them to the experimentally measured scattering parameters. A two-dimensional Newton-Raphson root search is used to minimize the difference between the theoretical and experimental S-parameters using the equations

$$\begin{aligned} \left| S_{11}^{\text{thy}}(\omega, \epsilon, \mu) - S_{11}^{\text{exp}}(\omega) \right| &< tol \\ \left| S_{21}^{\text{thy}}(\omega, \epsilon, \mu) - S_{21}^{\text{exp}}(\omega) \right| &< tol \end{aligned} \tag{5.1}$$

where it is accepted that the actual values of permittivity ϵ and permeability μ will drive the two functions of (5.1) below the specified tolerance.

5.1 Test Procedure

Microwave measurements were performed at room temperature in two frequency bands, S-band ($2.6 - 3.95$ GHz) and X-band ($8.2 - 12.4$ GHz). The room temperature characterizations were done on samples with deliberately machined gaps in order to simulate the effect of a high temperature waveguide expansion. Measurement of the physical dimensions of the samples was performed in conjunction with the microwave measurements.

Room temperature tests of samples machined with a gap sufficiently mimicked the conditions of a high temperature test to the satisfaction of the research sponsor. All data, both at S- and X-band, was collected on a Hewlett-Packard 8510C Network Analyzer located at the AFIT Microwave Lab between the months of November 2006 and February 2007. The measurement apparatus for S- and X-band can be seen in Figure 5.1 and Figure 5.2, respectively. A Thru-Reflect-Line (TRL) calibration scheme was used to calibrate out the sample holder.

The results presented are the characterization of two materials, acrylic and FGM-125. The acrylic material is a commercially available, ideally lossless dielectric. FGM-125 is a commercially available rubberized magnetic shielding material, having both electric and magnetic losses, manufactured by Emerson & Cuming. Measurements of the acrylic were only done at S-band, while FGM-125 was measured at S-band and X-band. This research is intended specifically for magnetic materials, but it can be applied generally, hence the inclusion of the acrylic measurements.

Parameter data is presented visually using the convention $\epsilon_r = \epsilon' - j\epsilon''$ and $\mu_r = \mu' - j\mu''$. Truth data was calculated using NRW on a measurement of a sample that completely filled the waveguide. RPI was not used to calculate the truth data, since it is not a standard measurement technique. The uncorrected data is the raw data of the PFW measurement, and NRW is used to extract the effective permittivity and permeability of this measurement. Additionally, the minimization equations of (4.63) are used in conjunction with PFW theory to characterize samples using the reference plane independent formulation. The corrected data corresponding to this method is labeled RPI. The RPI correction is always calculated with the same number of modes as the standard mode-matching correction.

5.1.1 Error Analysis. Throughout the course of the research, every attempt was made to minimize conceivable sources of error. The well-known TRL technique was used to calibrate the waveguide/HP 8510 system, minimizing systematic instrumentation uncertainty. The waveguides were mounted on fixed racks to minimize unnecessary movement of cables and prevent accidental shifting of the sample in the sample holder (see Figures 5.1 and 5.2). The use of precision alignment pins between the waveguide flanges and sample holder ensured consistency of the system during calibration and measurements.

One unavoidable source of error was the measurement of the physical dimensions of each sample under test. Using calipers with ± 2 mil accuracy, each sample dimension (width, height, thickness) was measured five times, and the average value

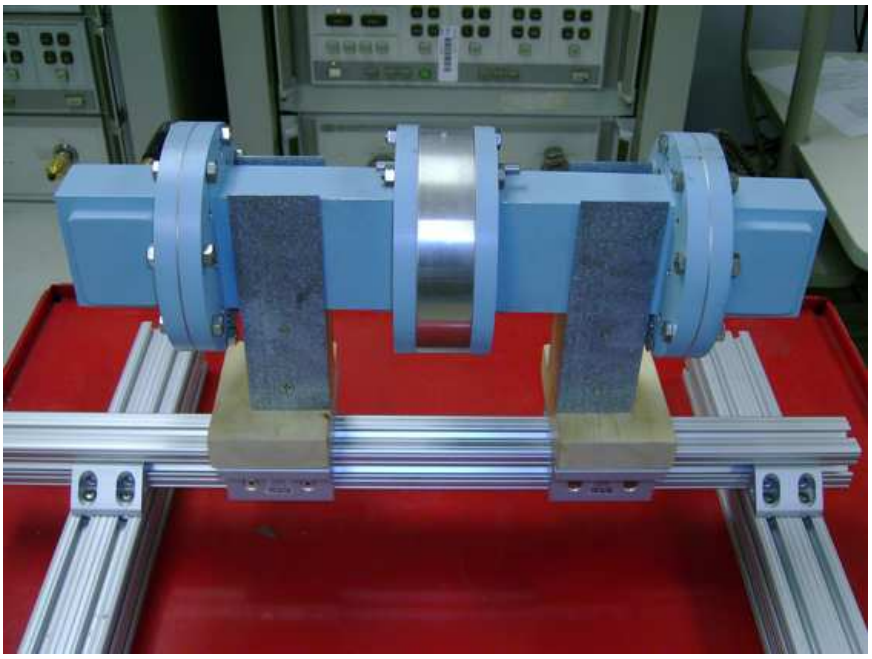

Figure 5.1: Mounted S-band waveguide attached to HP 8510 Network Analyzer. The mounting rack minimizes unnecessary movement of the cables.

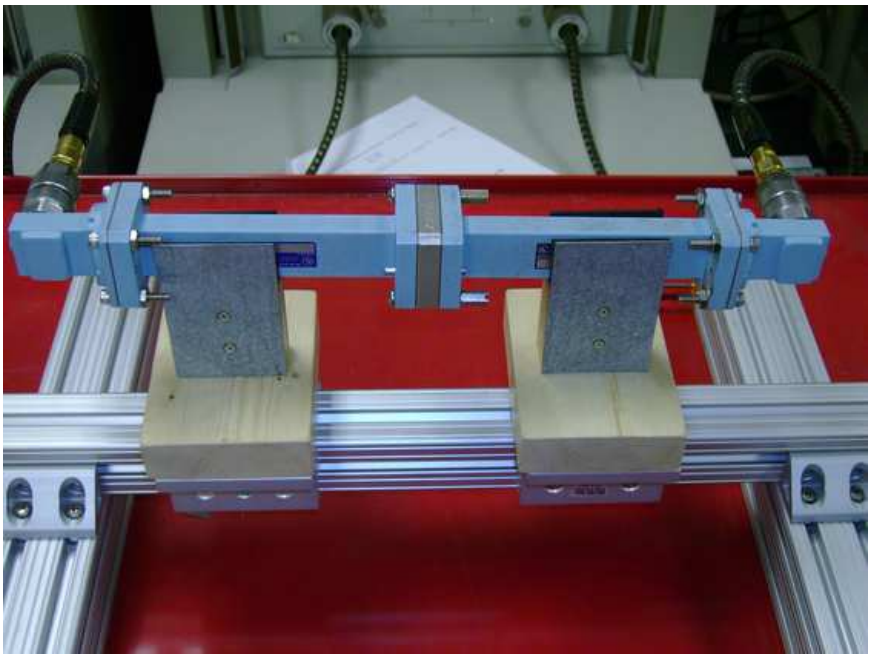

Figure 5.2: Mounted X-band waveguide attached to HP 8510 Network Analyzer

was recorded. A differential error analysis was performed to determine the effect of uncertainty in height h and thickness d on the final calculation of permittivity and permeability.

It has been suggested that the real and imaginary components of permittivity and permeability be described as functions of h and d [12,13]. However, this choice of functions does not reflect the mechanics of the algorithm itself, since the actual solution set is theoretical S-parameters. An error analysis of the S-parameters themselves would not be particularly useful, since the purpose of the research is to calculate ϵ and μ. Therefore, the error analysis of ϵ and μ will consider propagation of uncertainty in the calculated S-parameters due to the measurement uncertainty in sample height and thickness.

Let κ be either relative permittivity or permeability, such that

$$\kappa = \kappa'(h,d) - j\kappa''(h,d)$$

The real part of the calculated material parameter due to a height h and thickness d is expanded in a Taylor series around the point h_0 and d_0,

$$\kappa'(h_0+\delta h, d_0+\delta d) = \kappa'(h_0,d_0) + \frac{\partial\kappa'(h_0,d_0)}{\partial h}\delta h + \frac{\partial\kappa'(h_0,d_0)}{\partial d}\delta d + ... \qquad (5.2)$$

where δh and δd are the measurement uncertainties (± 2 mils) in height and thickness, respectively. The higher order terms of the Taylor series can be neglected since the uncertainty is so small. The total uncertainty in κ' can now be approximated by

$$\delta\kappa' = \kappa'(h_0+\delta h, d_0+\delta d) - \kappa'(h_0,d_0) \approx \frac{\partial\kappa'(h_0,d_0)}{\partial h}\delta h + \frac{\partial\kappa'(h_0,d_0)}{\partial d}\delta d \qquad (5.3)$$

which represents the uncertainty contribution of both measurements. Since an analytic expression for the partial derivatives does not exist, they must be calculated via a numerical approximation. Using forward differences, the two partial derivatives of

(5.3) are

$$\delta\kappa'_h = \frac{\partial\kappa'(h_0,d_0)}{\partial h}\delta h \approx \frac{\kappa'(h_0+\delta h,d_0)-\kappa'(h_0,d_0)}{\delta h}\delta h = \kappa'(h_0+\delta h,d_0)-\kappa'(h_0,d_0)$$
$$\delta\kappa'_d = \frac{\partial\kappa'(h_0,d_0)}{\partial h}\delta h \approx \frac{\kappa'(h_0,d_0+\delta d)-\kappa'(h_0,d_0)}{\delta d}\delta d = \kappa'(h_0,d_0+\delta d)-\kappa'(h_0,d_0)$$

The quantities δh and δd can in general be positive or negative, but this analysis will proceed considering the compounded uncertainty of overmeasuring both sample dimensions. While all the errors, assuming they are independent and random, could be combined in quadrature, a worst-case approximation is

$$|\delta\kappa'| = |\delta\kappa'_h + \delta\kappa'_d| < |\delta\kappa'_h| + |\delta\kappa'_d| \tag{5.4}$$

The Triangle Inequality shows that the absolute value of the sum of the errors is always less than the sum of the absolute values [25]. Substituting the real and imaginary parts of ϵ and μ in for κ completes the error analysis.

The height iteration method used to solve the eigenvalue equation for the correct value of the complex propagation constant γ_z in the PFW region is, unfortunately, not consistently stable. Providing an initial guess of γ_{FFW} for a particular mode does not guarantee that the root search for γ_{PFW} will converge on the next consecutive root, if it converges at all. It is also possible that the root search will find the same root twice, or skip a root. If this happens, the subsequent filling of the mode matrix in (4.56) will be inaccurate, due to the use of incorrect values of γ_z. Verification of sample homogeneity is also beyond the scope of this research, so it is assumed that material samples are homogeneous.

5.2 Room Temperature PFW Results

5.2.1 Acrylic. Although this mode-matching technique is meant to be applied to magnetic materials, a correction can be applied to a dielectric material in order to verify that the algorithm is working. Therefore, acrylic samples were ob-

tained from the AFIT machine shop, manufactured to the dimensions shown in Table 5.1. Acrylic is non-magnetic, so it was assumed that the sample permeability is that

Table 5.1: Acrylic Samples, S-Band

Sample #	Thickness (in)	Width (in)	Height (in)	Effective Gap (±2 mils)
1	0.24	2.84	1.340	0
2	0.24	2.84	1.328	12

of free space. The PFW correction was performed on Sample 2, measured to have an effective air gap of 12 mils. A correction using 5 modes was performed, with the results for real permittivity displayed in Figure 5.3. Acrylic is essentially lossless ($\epsilon'' \approx 0$), so the imaginary component is not presented graphically. The corrected permittivity is within 2% of the true value for the entire band, and provides a noticeable improvement over the uncorrected data. When combined with the RPI formulation (also using 5modes), the correction is nearly perfect.

Having shown the performance of the correction for this simple case, it is now appropriate to consider the more complex situation of magnetically lossy material.

5.2.2 FGM-125. Samples of FGM-125 were obtained and machined to the dimensions shown in Table 5.2, to be used in tests at S-band (2.6 - 3.95 GHz). In addition, samples were machined to the dimensions shown in Table 5.3 to be used in tests at X-band (8.2 - 12.4 GHz). The S-band results will be discussed first.

Table 5.2: FGM-125 Samples, S-Band

Sample #	Thickness (±2 mils)	Width (in)	Height (in)	Effective Gap (±2 mils)
1	125	2.84	1.340	0
2	125	2.84	1.313	27
3	125	2.84	1.259	81

Sample 1, which completely filled the waveguide cross section, was used as the reference sample. A 10 mode correction was applied to Sample 2, measured with a 27 mil top air gap. In Figures 5.4 and 5.5, it can be seen that while the true complex permittivity is reasonably constant across the frequency band, permeability is not.

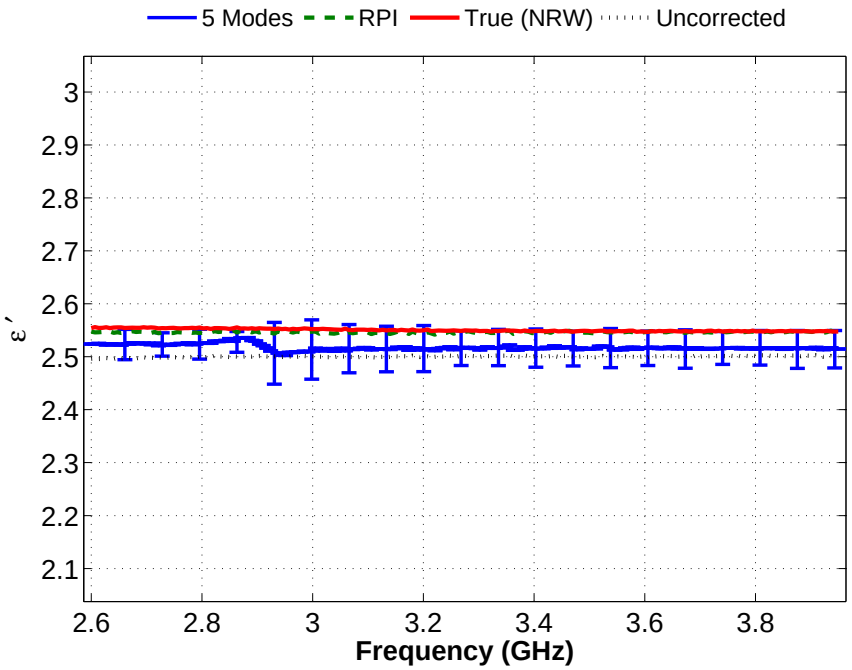

Figure 5.3: Measured real permittivity of acrylic with 12 mil air gap. Acrylic is both lossless and non-magnetic, so it is assumed $\epsilon'' = 0$ and $\mu_r = 1$. A 5 mode correction provides a significant improvement. The addition of the RPI-technique results in a nearly perfect correction. Error bars indicate ± 2 mil uncertainty in height and thickness.

Table 5.3: FGM-125 Samples, X-Band

Sample #	Thickness (±2 mils)	Width (in)	Height (in)	Effective Gap (±2 mils)
1	125	0.90	0.40	0
2	125	0.90	0.39	10
3	125	0.90	0.35	45

This is an expected property of magnetic materials, that both μ' and μ'' tend to decrease quickly for increasingly high frequencies [21].

From Figure 5.4 (a), it is apparent that the ϵ' extraction is highly sensitive to gap size, since the uncorrected measurement is consistently 8% below the true data. The modal correction, both with and without the RPI formulation, converges to a slightly higher value of real permittivity, just outside the range of the error bars, within 5% of the truth data. The uncorrected data for ϵ'' is sufficiently close to the true value of zero, so a modal correction is not actually necessary. However, it can be seen that inclusion of RPI yields a superior result than when it is neglected.

Examining the plots of real and imaginary permeability in Figure 5.5 it can be seen that these measurements are not as sensitive to top/bottom air gap, given the proximity of the uncorrected data to the truth data. The 10 mode correction does not much improve the extraction for either real or imaginary parts, although using RPI has a considerable effect, especially for the imaginary component.

In a lab environment, it is expected that the waveguide samples will not be deliberately machined with large gaps. Even in a high temperature measurement, unless the sample falls over onto its side, extremely large gaps are not expected. However, in order to illustrate a more drastic case of a PFW, and to test the accuracy of the modal method for large gaps, Sample 2, with a gap of 81 mils was tested. As the largest gap size under test, it will be easier to see the benefit of including successive higher-order in the mode-matching correction. Therefore, a 10 mode correction is presented in Figure 5.6 and Figure 5.7.

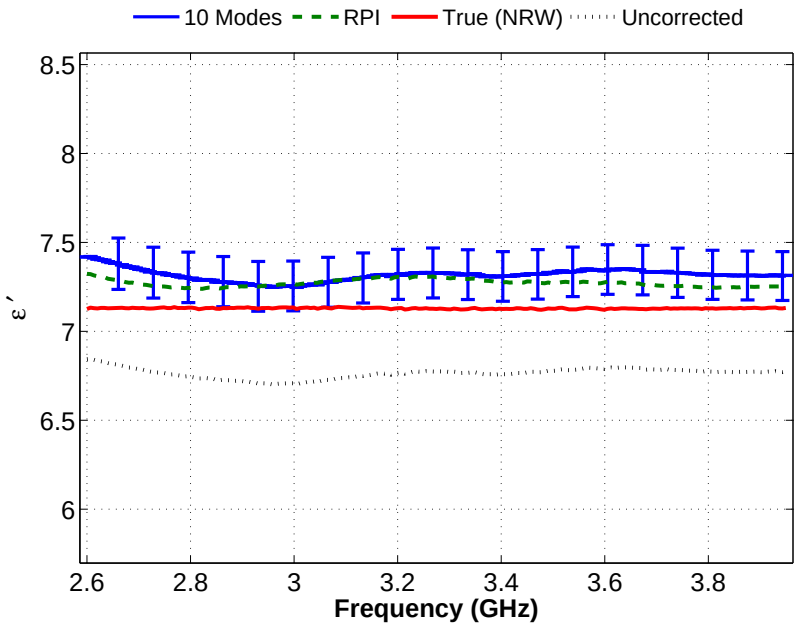

(a)

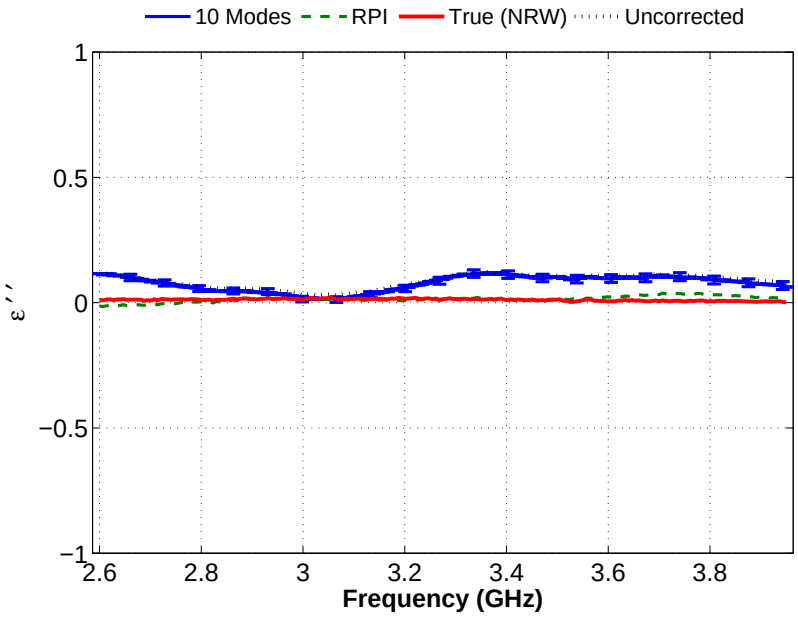

(b)

Figure 5.4: Permittivity of FGM-125 in a PFW with 27 mil top air gap. A 10 mode solution overcorrects the (a) real part, and yields an exact match between 3 and 3.1 GHz for the (b) imaginary part. The inclusion of RPI is within the error bounds in (a), but gives superior performance in (b). Error bars indicate ±2 mil uncertainty in height and thickness.

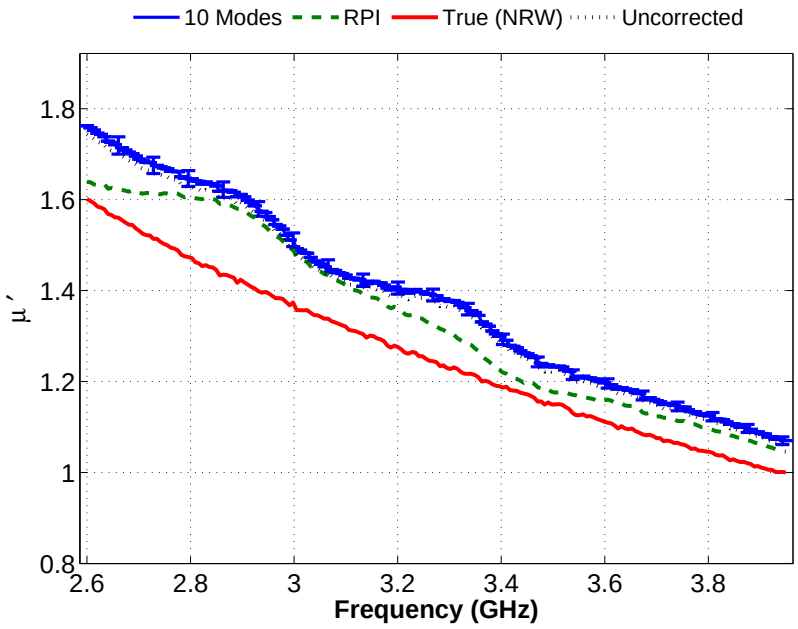

(a)

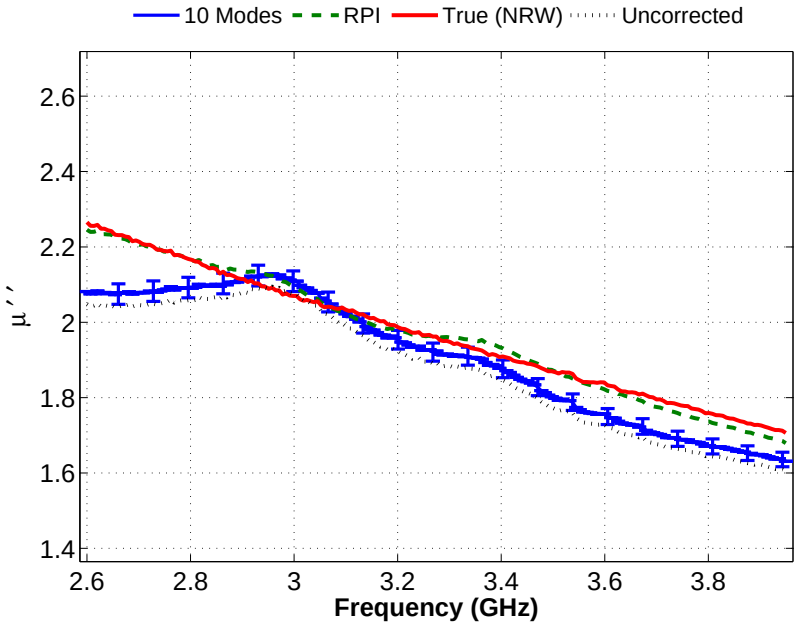

(b)

Figure 5.5: Permeability of FGM-125 in a PFW with 27 mil top air gap. Correction using 10 modes has almost no difference from the uncorrected data for either the (a) real or (b) imaginary components. The RPI, however, is an improvement to both components, and is nearly exact for μ''. Error bars indicate ± 2 mil uncertainty in height and thickness.

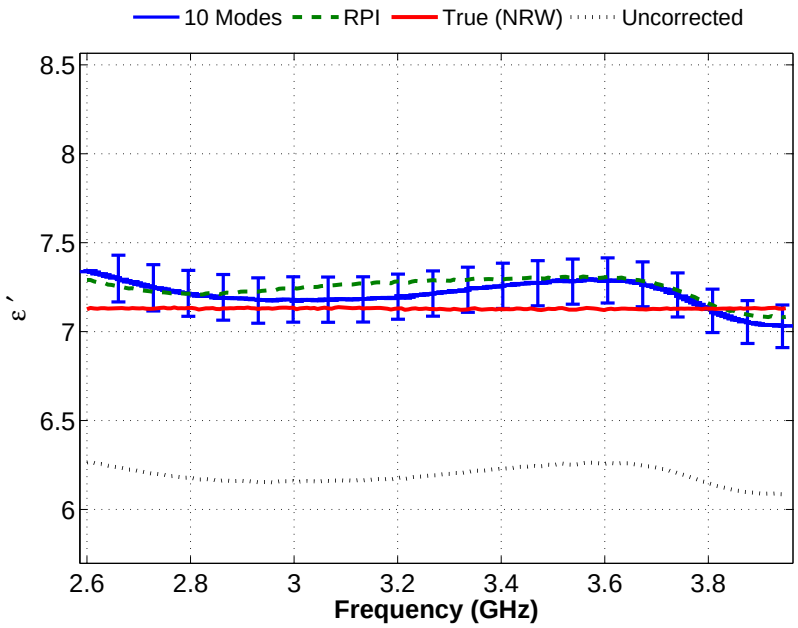

(a)

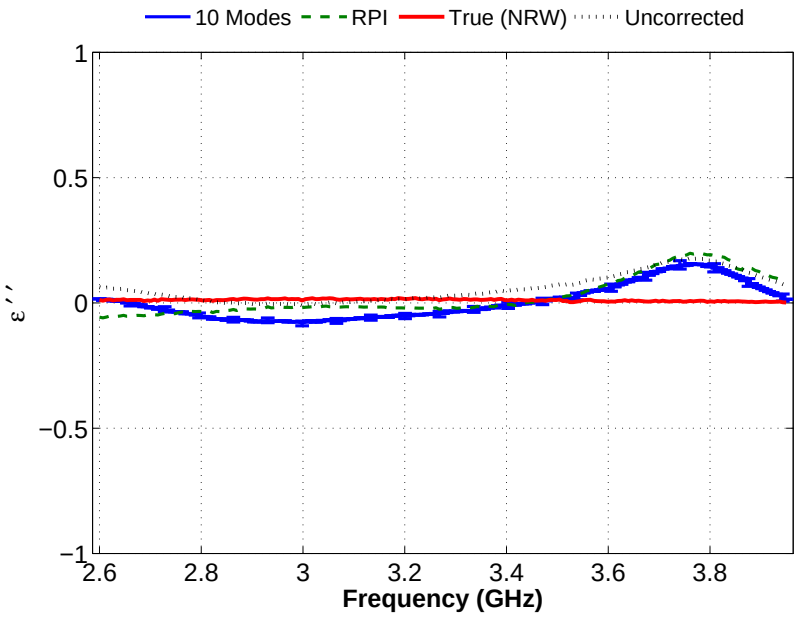

(b)

Figure 5.6: Permittivity of FGM-125 in a PFW with 81 mil top air gap. 10 mode correction applied. (a) Use of RPI is within the error bounds of the 10 mode correction for ϵ'. (b) All extractions are reasonably similar. Error bars indicate ± 2 mil uncertainty in height and thickness.

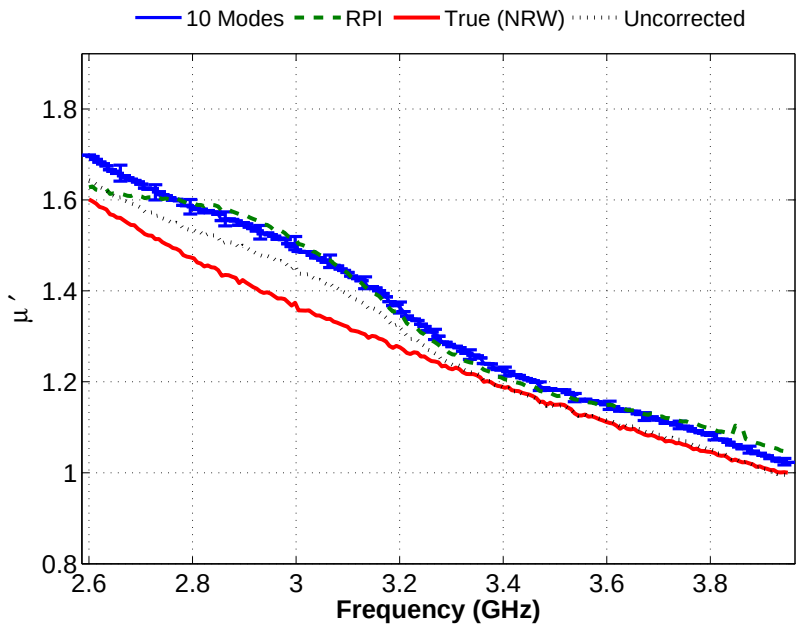

(a)

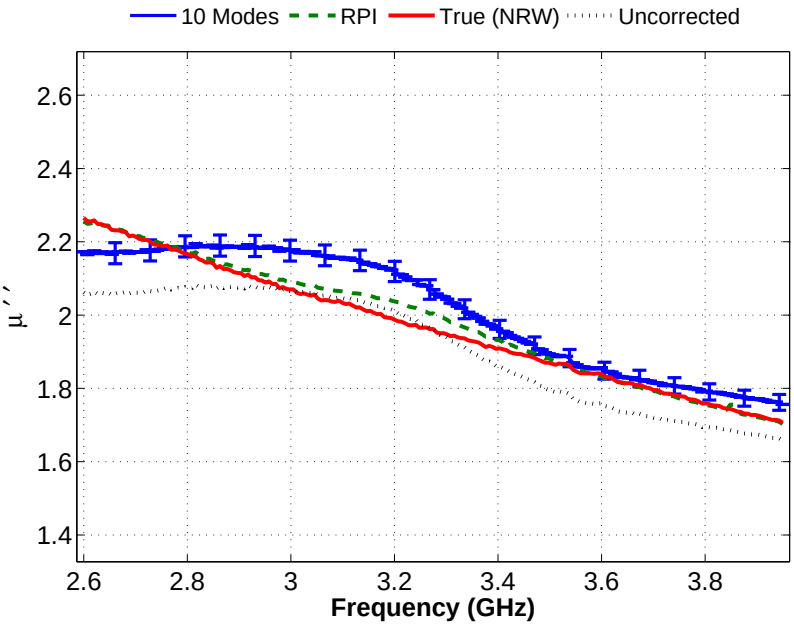

(b)

Figure 5.7: Permeability of FGM-125 in a PFW with 81 mil top air gap. 10 mode correction applied. (a) Neither correction improves upon the raw data. (b)Use of RPI gives better results than the modal correction alone, nearly perfect alignment with the truth data. Error bars indicate ±2 mil uncertainty in height and thickness.

The correction of ϵ' in Figure 5.6 (a) yields excellent results, as the truth data is within the uncertainty of the modal correction, both with and without the RPI formulation. Considering the correction to ϵ'' in Figure 5.6 (b), once again the uncorrected data yields an acceptable value. Of the modal correction methods, however, RPI is the preferred solution , since it provides the most improvement. Likewise, in Figure 5.7, the use of RPI is preferred as a correction to μ', and μ''.

The difference between the uncorrected permittivity data of the 27 mil gap (Figure 5.4 (a)) and the 81 mil gap, and the relative stability of the other three complex parameters, is a further indication of the sensitivity of permittivity extractions to this particular PFW geometry. This is due to the field pattern in the PFW region.

The electric field vector e_y is discontinuous in $\hat{y}$ between the material and free space, creating a capacitive charge distribution [22]. The measurement of electric permittivity, therefore, is very sensitive to this geometry. However, the magnetic field vector h_x, for a given value of y, is continuous in $\hat{x}$. Accordingly, the measurement of magnetic permeability is much more stable than the permittivity measurement for top air gaps. If, for example, the air gap was located in the other dimension (i.e. left/right), an inductive charge distribution would be created. It can reasonably be assumed that in this scenario, the permeability measurement would suffer more than permittivity, using similar reasoning.

The second round of room temperature measurements were performed at X-band, using the samples described by Table 5.3. The parameters extracted using NRW on measurements of Sample 1, the fully filled case, are assumed to be the truth data. The first measurements were taken of Sample 2, with a single top air gap of 10 mils. A 10 mode correction is presented in Figures 5.8 and 5.9.

The real permittivity extraction of Figure 5.8 (a) represents an unsuccessful attempt to improve ϵ', as both corrections are less than the truth data. This may be due to a strong capacitive effect at the measurement frequency. The corrected and uncorrected data sets corresponding to ϵ'' in Figure 5.8 (b) are nearly identical

throughout the entire band, which is consistent with previous measurements. The 10 mode correction, when applied to magnetic permeability, is very accurate, having better performance than the RPI formulation, which can be verified in Figure 5.9. It must also be pointed out that the 2 mil uncertainty in height and thickness has almost no effect on extraction of permeability. This is in contrast to permittivity, which is clearly seen to be affected by a small amount of uncertainty in the specified sample dimensions.

Sample 3, having a top gap of 45 mils, was also tested. A 15 mode correction was used, and the results are displayed in Figures 5.10 and 5.11. The extraction of ϵ', in Figure 5.10 (a), reveals that use of the 15 mode correction gives a dramatic improvement over the increasingly worse uncorrected data. However, even when combined with the RPI formulation, the correction is not stable across the entire band. The standard mode correction would be preferred in this case, since it has a better average value and the average RPI value is too low.

The extraction of ϵ'' in Figure 5.10 (b) is the first instance when the uncorrected data did not accurately approximate the truth data. In addition, the two modal corrections show significant variation with frequency. This may be due in part to the instability of the Newton-Raphson Root search when used in parameter extractions on lossless materials. It is well known that "good" guesses are critical when using this algorithm [1, 13]. Of the corrections to permeability, shown in Figure 5.11, the mode-matching correction using RPI was superior for both μ' and μ''.

5.2.3 Complex Propagation Wave Number. It has been mentioned that a valid PFW correction is contingent upon satisfaction of the transcendental equation

$$\frac{k_{y1}}{\epsilon_1}\sin k_{y1}h\cos k_{y2}(b-h)+\frac{k_{y2}}{\epsilon_2}\sin k_{y2}(b-h)\cos k_{y1}h=0 \tag{5.5a}$$

$$\gamma_{z,1n}^2=k_{y1,n}^2+k_x^2-k_1^2=k_{y2,n}^2+k_x^2-k_0^2$$

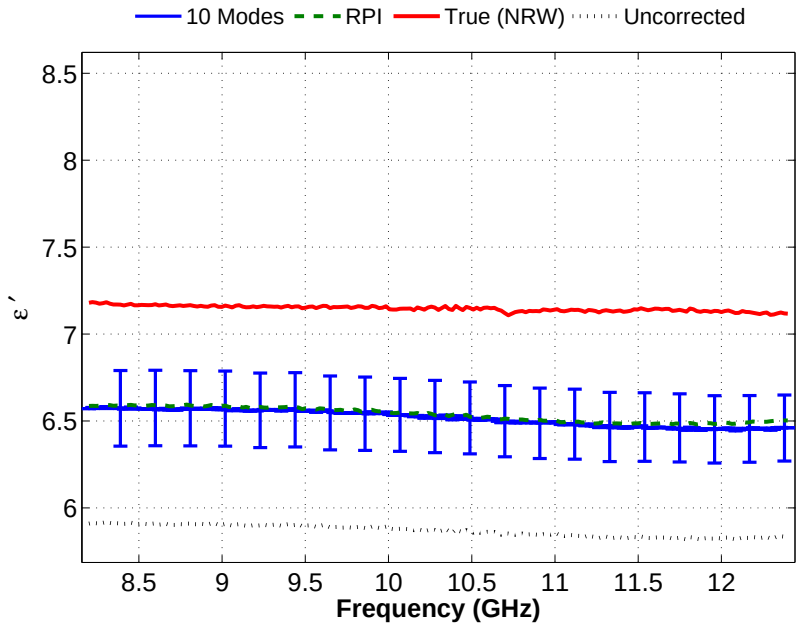

(a)

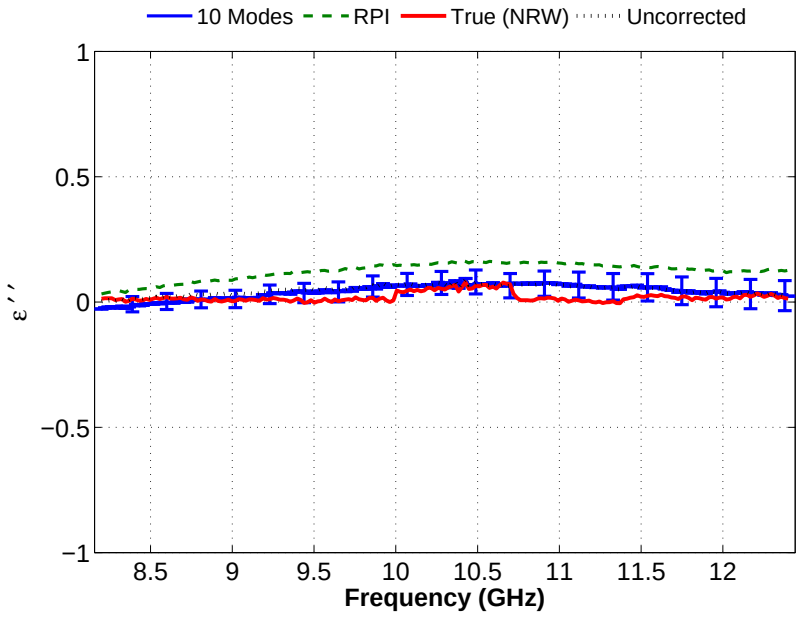

(b)

Figure 5.8: Permittivity of FGM-125 in a PFW with 10 mil top air gap. A 10 mode correction is given. Error bars indicate ±2 mil uncertainty in height and thickness. (a) Both corrections are unusable, although are preferred to the uncorrected data. (b) The modal correction and the uncorrected data are closest to the truth data.

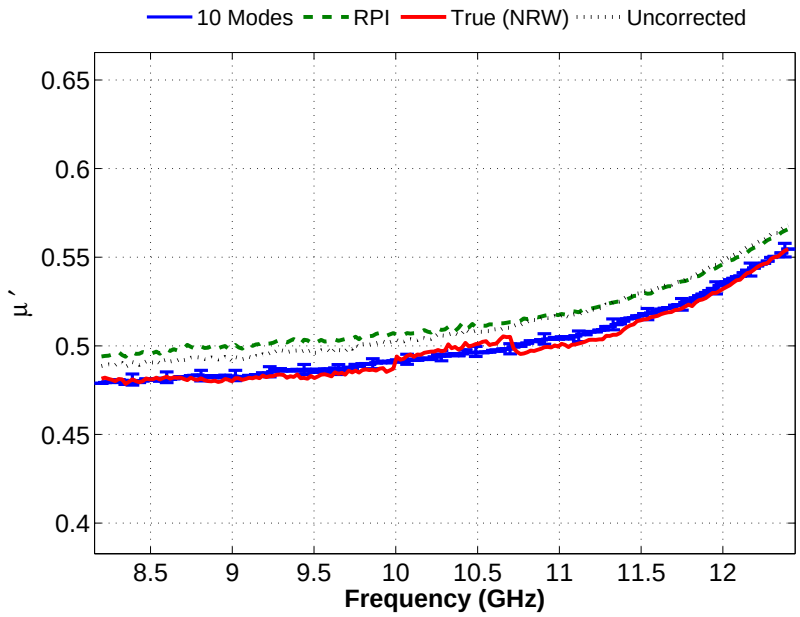

(a)

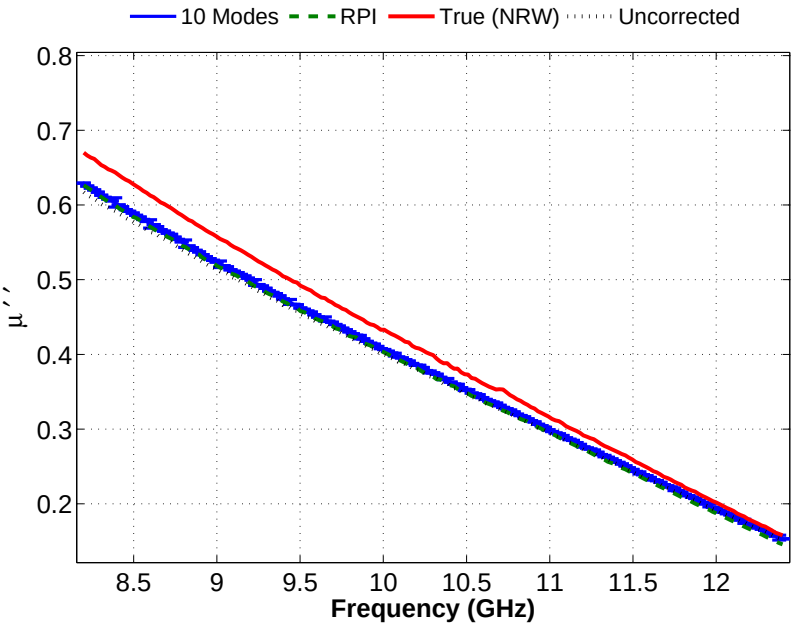

(b)

Figure 5.9: Permeability of FGM-125 in a PFW with 10 mil top air gap. A 10 mode correction is given. (a) Non-RPI modal correction is nearly exact. (b) All three data sets are equally close to the truth data.

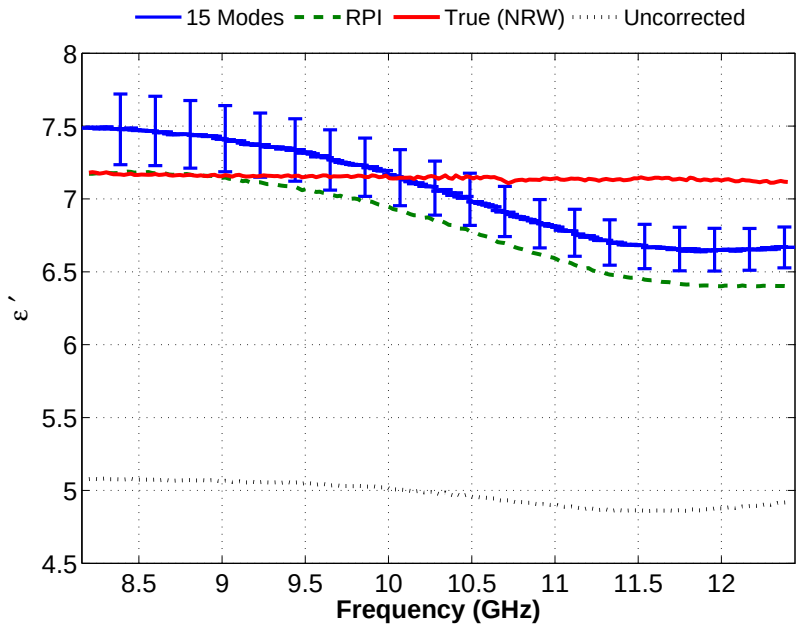

(a)

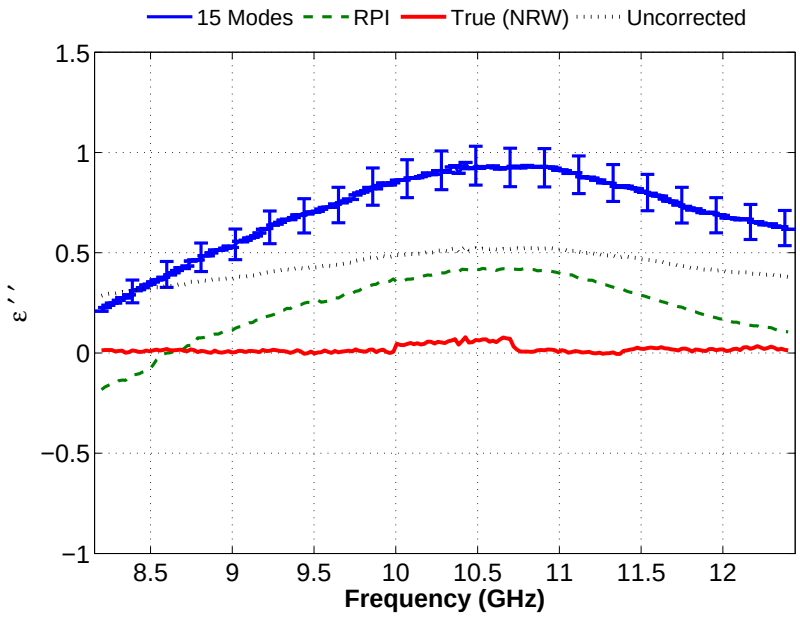

(b)

Figure 5.10: Permittivity of FGM-125 in a PFW with 45 mil top air gap. A 15 mode correction is given. (a) Although both mode corrections are in the vicinity of the truth data, the non-RPI is preferred. (b) The RPI correction is the best of the 3 data sets, but still varies significantly from the truth data.

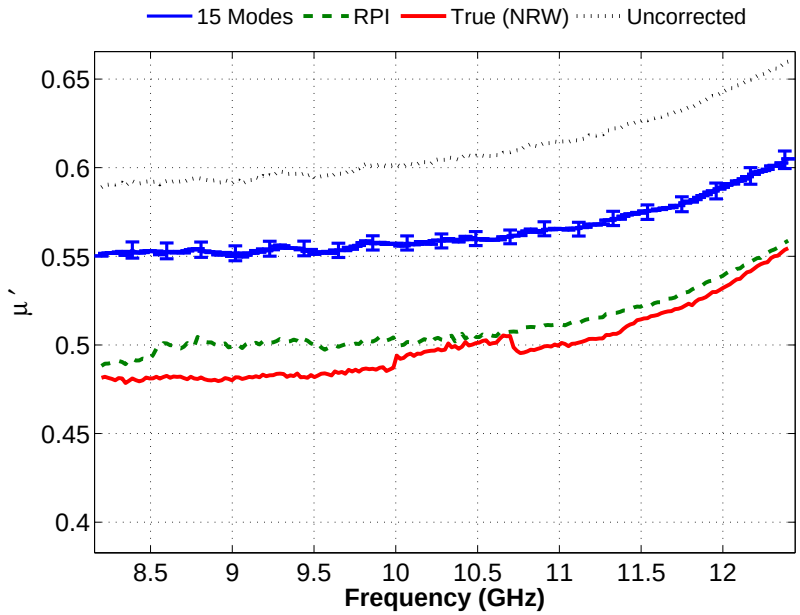

(a)

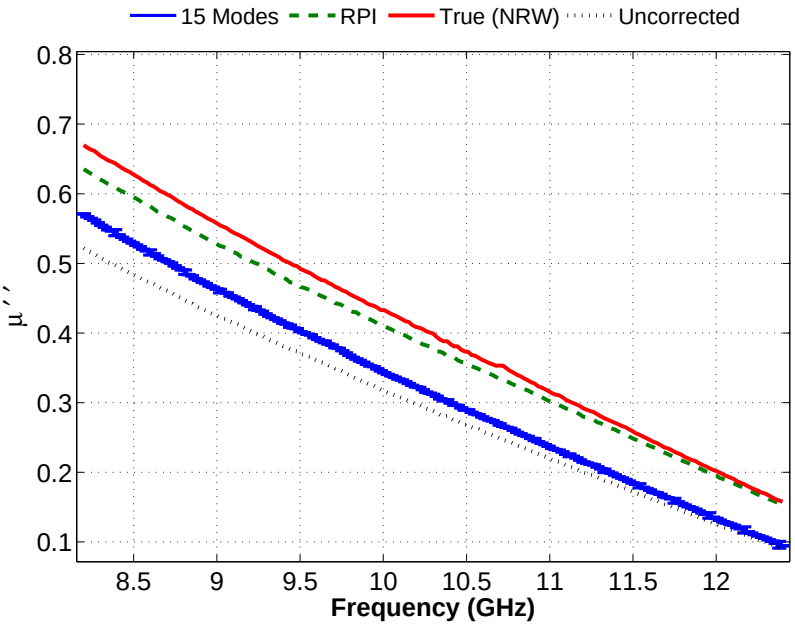

(b)

Figure 5.11: Permeability of FGM-125 in a PFW with 45 mil top air gap. A 15 mode correction is given. (a,b) Use of RPI gives the best correction, as the non-RPI is closer to the uncorrected data.

which, through finding γ_z, enables the determination of the wave numbers k_{y1} and k_{y2}. Using the procedure outlined in Section 4.2.6, an initial guess of γ_{FFW}, the propagation wave number of a fully filled waveguide, is provided to the root search. It is trivial to calculate γ_{FFW} for any number of desired modes, since it is based on the waveguide geometry. However, using a numerical method to determine γ_{PFW} may lead to erroneous results, due to instability in the iteration.

Therefore, it is useful to observe the response of the mode-matching correction as successive modes are included in the analysis. This will be done with FGM-125 Sample 3 (S-band), having an air gap of 81 miles. Corrections to ϵ_r and μ_r using 1, 2, 3, 6 and 10 modes are illustrated in Figures 5.12 and 5.13. In Figure 5.12 (a), it is clearly seen that the uncorrected permittivity obtained using NRW is far below the true value rendering it completely inaccurate. Using the mode-matching technique with 1 mode (i.e. no higher-order modes) yields a small improvement. Adding 1 higher order mode improves the measurement further. Including 2 higher order modes (i.e. 3 modes total) results in an overcorrection, but as more modes are considered, the modal correction moves closer to the true value. Similar observations can be made about the ϵ'' correction in Figure 5.12 (b), although in that case the uncorrected data is closest to the truth data. This is also true for the corrections to μ' and μ'' in Figure 5.13.

The question remains as to the reason for the mode-matching overcorrection of ϵ' in Figure 5.12 (a). Recall that the values of the propagation wave number γ are obtained from satisfaction of the eigenvalue equation (5.5a). In order to observe the behavior of the eigenvalue equation in the complex plane, two surface plots are presented in Figure 5.14. The material under test is FGM-125, observed at 3.2 GHz, using two different air gap sizes: 27 mils and 81 mils, which correspond to Sample 2 and Sample 3 respectively.

The ratio of α to β, or the propagation - attenuation ratio, for each root of γ from Figure 5.14 is given in Table 5.4. A small ratio, such as that for mode 1 of the

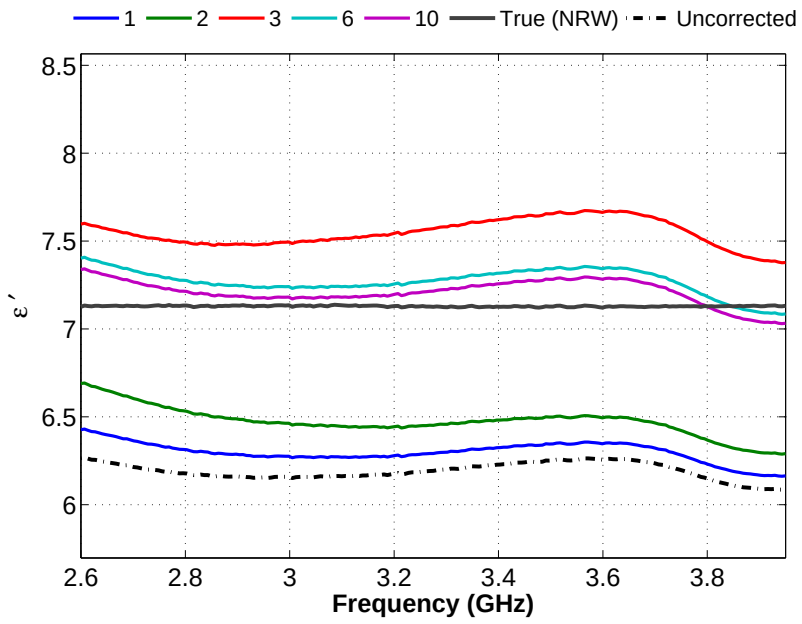

(a)

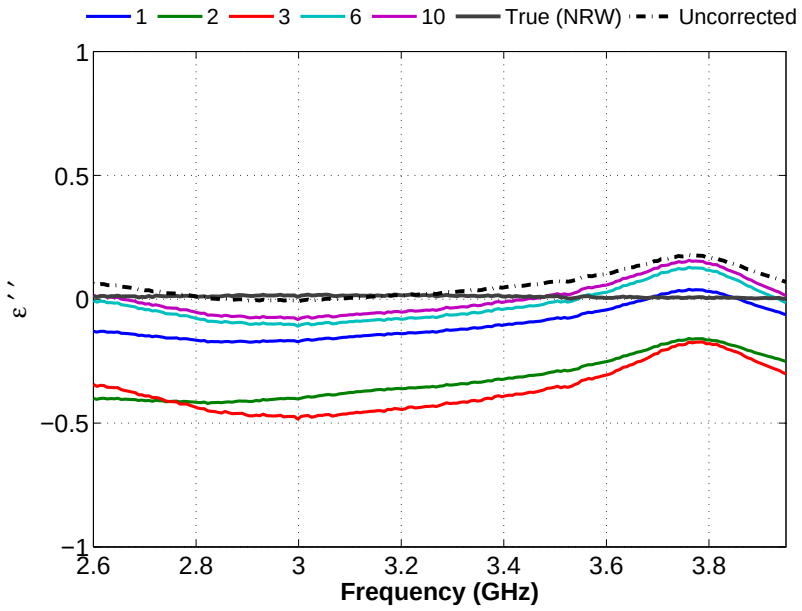

(b)

Figure 5.12: Permittivity of FGM-125 in a PFW with 81 mil top air gap. Multiple mode corrections are given. (a) Too few modes (e.g. 3) is an "overcorrection", but as more modes are included the correction rights itself. (b) Similar to (a), it is better to use more modes than too few. Uncorrected data gives the best result.

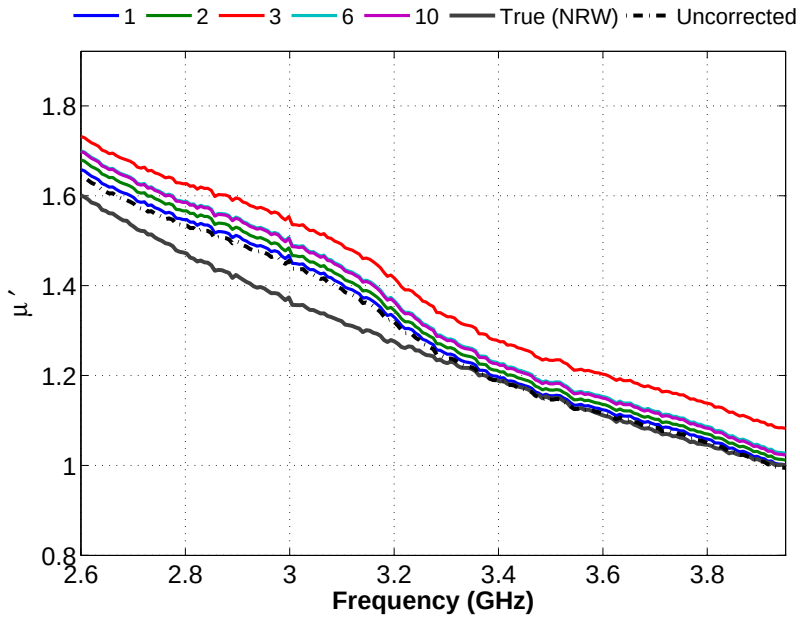

(a)

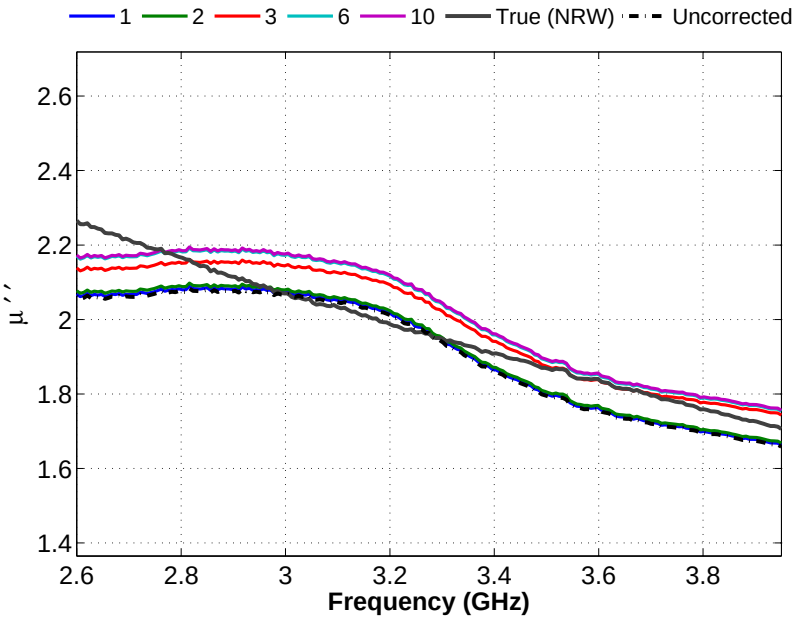

(b)

Figure 5.13: Permeability of FGM-125 in a PFW with 81 mil top air gap. Multiple mode corrections are given. (a) Minimal improvement from using increasing numbers of modes, but the overcorrection described in Figure 5.12 occurs here as well. (b) Uncorrected data again gives the best results, and is nearly identical to the 1 & 2 mode correction.

27 mil gap, indicates the the mode is highly propagating, whereas a large ratio, such as that for mode 5, indicates strong attenuation.

It is expected that the the dominant mode in a PFW system will have a small propagation-attenuation ratio, and this can be verified in Figure 5.14 (a), where the dominant mode can clearly be identified. The fact that the higher order mode roots in (a) are close to zero indicates minimal propagation. This is similar to the behavior of modes in a fully filled guide, in which the higher order modes (if they even exist) attenuate rapidly.

However, for the 81 mil gap case in Figure 5.14 (b), the situation is very different. Both the real and imaginary components of the roots are much larger than in (a). This causes the α-β ratio at every mode, except the first, to be much smaller than the 27 mil gap case. The first mode has 7 times the attenuation of the 27 mil gap dominant mode, so it can immediately be recognized that each γ, especially in the large gap scenario, is both highly propagating and highly attenuated. The combination of these effects implies that many higher order modes are necessary for a proper correction using the PFW mode-matching technique. This is consistent with the observations made of the successive mode corrections of Figures 5.12 and 5.13. Including several higher order modes balances the total field, which leads to a more accurate correction.

Table 5.4: Propagation - Attenuation Ratios

	FGM-125 27 mil gap			FGM-125 81 mil gap		
Mode #	α	β	$\frac{\alpha}{\beta}$	α	β	$\frac{\alpha}{\beta}$
1	11	40	0.3	259	125	2.1
2	117	12	9.8	325	109	3.0
3	232	5	46.4	394	90	4.4
4	347	3	115.7	464	77	6.0
5	461	2.8	164.6	534	67	8.0

The potential exists for instability in the numerical root search algorithm used to converge to roots of the eigenvalue equation. If the solution space has a shallow gradient, such in some regions of Figure 5.14 (b), the Newton-Raphson method (which

uses a tangent line to approximate the next guess) may obtain a poor approximation. It also is helpful if the roots are clearly distinguishable from one another, as in Figure 5.14 (a). In cases where the roots are very close together, or do not stand out greatly from the surrounding space, it may be appropriate for a different root search, such as the Muller Method, to be used [1, 13], although this step was not taken here.

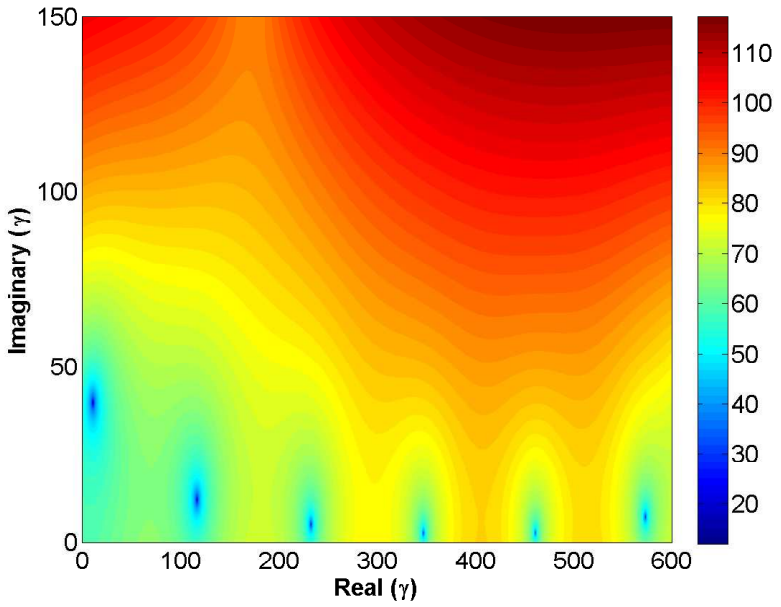

(a)

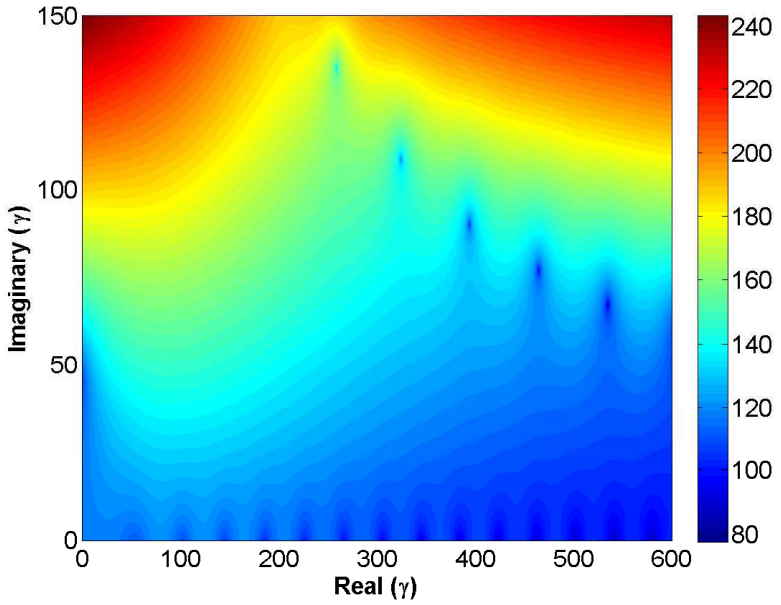

(b)

Figure 5.14: Two surface plots of the eigenvalue equation over the complex plane, for which the true PFW γ will force the output to zero. Material under test is FGM-125, observed at 3.2 GHz. Results are presented in logarithmic scale. (a) Sample 2, 27 mil air gap, first 6 PFW modes. The imaginary part, or phase constant, is close to zero, or cutoff, for the last 4 modes. This ordering resembles a plot of γ that would be expected in a FFW. (b) Sample 3, 81 mil air gap, first 5 PFW modes. Roots of γ have large real and imaginary components, indicating both high attenuation and also strong propagation.

VI. Conclusions and Recommendations

This thesis has demonstrated the feasibility of using modal analysis to accurately perform electromagnetic material characterization in a partially filled waveguide. Waveguide expansion is a common problem in high-temperature material measurements, since gaps form between the sample and waveguide walls. This discontinuous geometry excites higher order which are not accounted for in algorithms such as Nicolson-Ross-Weir. A correction was accomplished by considering a single air gap between the top of the sample and the waveguide. Because the waveguide is partially filled in the y-axis, the scattered mode set can be completely described using TM^y modes.

Using Maxwell's equations it was shown that the transverse field vector e_x was linearly dependent on the derivatives of e_y and h_x. Therefore, the the boundary condition between the empty and partially filled waveguide regions depended only on explicitly matching the transverse e_y and h_x mode vectors, although continuity of e_x can be shown numerically. A 2-dimensional Newton-Raphson root search was used to compute the required value of the complex propagation constant γ_z of each higher order mode in the partially filled waveguide, which was then used to construct a finite number of field modes in the system. The theoretical scattering parameters of this system are extracted and compared to the experimental scattering parameters in a minimization equation. The top-level root search uses the minimization equations to converge to the true values of relative permittivity and permeability of the sample.

Measurements of acrylic and magnetic shielding material in a PFW geometry were performed at room temperature in S-band and X-band. For most air gaps, acceptable corrections, i.e. within 10% of the true value, could usually be achieved using 15 modes or less. At S-band, modal corrections for air gaps greater than 100 mils did not converge. Modal corrections on the 45 mil gap, the largest gap at X-band, did not converge using more than 10 modes.

It was difficult to obtain useful modal corrections of the large gap PFW acrylic samples. Even when using a single transmission measurement to extract permittivity, i.e. a 1-D search, the near-lossless property of the sample made the root searching

unstable, and no amount of modes used in the correction would converge. Corrections to air gaps in magnetic shielding material measurements were usually more successful, unless a significant gap (60-100 mils) was present. In most cases, the algorithm could be expected to compute the entire data set (201 points) in less than 20 minutes using a 15 mode correction.

The calculation of real permittivity (regardless of material) is more sensitive to a top air gap than either imaginary permeability or real and imaginary permeability. This is due to the electric field vector discontinuity that exists across the material boundary, which does not exist in the two other transverse field vectors. Therefore, it is reasonable that the mode-matching technique will be most effective at correcting the parameter most corrupted by the presence of an air gap. If the gap was in the other dimension, i.e. left-right, it is expected that the permeability measurement would suffer. The modal correction was usually able to obtain an acceptable correction for ϵ' when ϵ'' was very small. The success of modal corrections to μ_r depended on the gap size and frequency range. It was not unusual for the "uncorrected" PFW data to be the most acceptable data set.

The addition of a reference plane independent formulation to the mode-matching technique contributed significant improvements to the correction. Foremost, this indicates that samples were not precisely aligned with the reference plane. Secondly, by using both forward and reverse scattering parameters, the effects of sample inhomogeneity on permittivity and permeability extraction is reduced. Based on these observations, it is recommended that future material characterizations include a reference plane independent solution method.

The experiment was not performed at high temperature, but is a presented as a proof of concept technique for a partially filled waveguide environment.

This research presents a novel method for characterization improvements in high temperature rectangular waveguide measurements. The foundation of the single air gap correction is a mode-matching technique of the dominant and higher order

scattered TM^y modes. The mode-matching is then combined with reference plane independence to eliminate possible phase shift errors. Finally, the method is applied to measurements involving a magnetic material. The combination of these components has not, to the best knowledge of the author, been presented before.

6.1 Future Work

It has been observed that a vital part of obtaining a correct solution using modal analysis is the accurate determination of the complex propagation constant γ_{PFW}. If an iterative search is used, care must be taken to ensure that "good" initial guesses are supplied to the algorithm. As an alternative, however, a root-search method which can identify and sort a desired number of mode propagation constants could be sought. Use of finite element analysis, genetic algorithms, or a less-sensitive iterative root search are possible options for improvement in this area. With more accurate values of γ_{PFW}, corrections for larger gaps can be calculated.

The top air gap PFW analysis should be combined with side air gaps to better simulate a high-temperature situation, since it is expected that all dimensions of the waveguide will expand. The room temperature tests had *a priori* knowledge of the dimensions, specifically the height, of the sample under test. This observation, however, cannot be made at high-temperature. It is recommended that known thermal expansion coefficients be combined with the PFW analysis to obtain a reasonably accurate guess for the air gap between the sample and waveguide while at high-temperature.

Appendix A. Nicolson-Ross-Weir Algorithm

Nicolson, Ross [23] and Weir [27] took expressions for the S_{11} reflection coefficient and S_{21} transmission coefficient and derived explicit formulas for the calculation of the material parameters permittivity and permeability (ϵ_r, μ_r). The derivation presented here pertains to use in a rectangular waveguide where $a \approx 2b$.

Given the scattering parameters S_{11} and S_{21}, the reflection coefficient R is given by

$$R = Q \pm \sqrt{Q^2 - 1} \tag{A.1}$$

where Q is

$$Q = \frac{(S_{11})^2 - (S_{21})^2 + 1}{2S_{11}} \tag{A.2}$$

The choice of sign in (A.1) which forces $|R| < 1$ is taken. Now, the transmission coefficient P is given by

$$P = \frac{S_{21}}{1 - R \cdot S_{11}} \tag{A.3}$$

The impedance z can also be found, as it is

$$z = \frac{1 + R}{1 - R} \tag{A.4}$$

In the rectangular waveguide, the propagation constant γ of the dominant, TE_{10} mode is

$$\gamma_0 = \sqrt{(k_x^2 - k_0^2)} \tag{A.5}$$

Finally, for a material sample of thickness d, relative permittivity and permeability can be given by the relations

$$\mu_r = \frac{-\ln(P) \cdot z}{\gamma_0 d} \tag{A.6}$$

$$\epsilon_r = \frac{k_x^2 - \left(\frac{\ln(P)}{d}\right)^2}{\mu_r k_0^2} \tag{A.7}$$

Appendix B. Integral Proofs

The integrals of Chapter IV are shown here in expanded form.

$$\begin{aligned} M_{np} &= \langle e_{y1n}, \psi_y \rangle \\ &= \int_y e_{y1n} \cdot \psi_y dy \\ &= \int_0^b \cos\frac{n\pi y}{b} \cos\frac{p\pi y}{b} dy \\ &= \int_0^b \cos^2\frac{n\pi y}{b} dy \\ &= \begin{cases} b/2, & n = p \\ 0, & n \neq p \end{cases} \end{aligned} \tag{B.1}$$

As a special case, if $n = 0$ (which would represent the dominant mode in the empty waveguide), (B.1) may be simplified to

$$\begin{aligned} M_{0p} &= \langle e_{y10}, \psi_y \rangle \\ &= \int_y e_{y10} \cdot \psi_y dy \\ &= \int_0^b \cos(0) \cos\frac{p\pi y}{b} dy \\ &= \int_0^b \cos^2(0)\, dy \\ &= \begin{cases} b, & n = p = 0 \\ 0, & n \neq p \end{cases} \end{aligned} \tag{B.2}$$

$$N_{np} = U_{np} + V_{np}$$

$$\begin{aligned}
U_{np} &= \langle \tilde{e}_{1,y1n}, \psi_y \rangle \\
&= \underbrace{\frac{\varepsilon_0}{\varepsilon_1} \frac{\cos\left(k_{y2}\left(b-h\right)\right)}{\cos\left(k_{y2}h\right)}}_{\zeta} \int_0^h \cos\left(k_{y1}y\right) \cos\frac{p\pi y}{b} dy \\
&= \frac{\zeta}{2} \int_0^h \cos\left(k_{y1} - \frac{p\pi}{b}\right) y + \cos\left(k_{y1} + \frac{p\pi}{b}\right) y dy \\
&= \frac{\zeta}{2} \left[\frac{\sin\left(k_{y1} - \frac{p\pi}{b}\right) y}{\left(k_{y1} - \frac{p\pi}{b}\right)} + \frac{\sin\left(k_{y1} + \frac{p\pi}{b}\right) y}{\left(k_{y1} + \frac{p\pi}{b}\right)} \right] \Bigg|_0^h \\
&= \frac{\zeta}{2} \left(\frac{\sin\left(k_{y1} - \frac{p\pi}{b}\right) h}{\left(k_{y1} - \frac{p\pi}{b}\right)} + \frac{\sin\left(k_{y1} + \frac{p\pi}{b}\right) h}{\left(k_{y1} + \frac{p\pi}{b}\right)} \right)
\end{aligned} \tag{B.3}$$

$$\begin{aligned}
V_{np} &= \langle \tilde{e}_{2,y1n}, \psi_y \rangle \\
&= \int_h^b \cos\left(k_{y2}\left(b-y\right)\right) \cos\frac{p\pi y}{b} dy \\
&= \frac{1}{2} \int_h^b \cos\left(k_{y2}b - k_{y2}y - \frac{p\pi y}{b}\right) + \cos\left(k_{y2}b - k_{y2}y + \frac{p\pi y}{b}\right) dy \\
&= \frac{1}{2} \int_h^b \cos\left(k_{y2}b - y\left(k_{y2} + \frac{p\pi y}{b}\right)\right) + \cos\left(k_{y2}b - y\left(k_{y2} - \frac{p\pi y}{b}\right)\right) dy \\
&= -\frac{1}{2} \left[\frac{\sin\left(k_{y2}b - y\left(k_{y2} + \frac{p\pi y}{b}\right)\right)}{\left(k_{y2} + \frac{p\pi y}{b}\right)} + \frac{\sin\left(k_{y2}b - y\left(k_{y2} - \frac{p\pi y}{b}\right)\right)}{\left(k_{y2} - \frac{p\pi y}{b}\right)} \right] \Bigg|_h^b \\
&= \frac{1}{2} \left(\frac{\sin\left(k_{y2}b - h\left(k_{y2} + \frac{p\pi y}{b}\right)\right)}{\left(k_{y2} + \frac{p\pi y}{b}\right)} + \frac{\sin\left(k_{y2}b - h\left(k_{y2} - \frac{p\pi y}{b}\right)\right)}{\left(k_{y2} - \frac{p\pi y}{b}\right)} \right)
\end{aligned} \tag{B.4}$$

$$P_{np} = \frac{1}{Z_{TM}} \langle e_{y1n}, \psi_y \rangle = \frac{1}{Z_{TM}} M_{np}$$
$$= \begin{cases} \frac{b}{2Z_{TM}}, & n = p \\ 0, & n \neq p \end{cases} \tag{B.5}$$

$$F_{np} = \frac{1}{\tilde{Z}_1} \langle e_{1,y1n}, \psi_y \rangle = \frac{1}{\tilde{Z}_1} U_{np}$$
$$= \frac{\zeta}{2\tilde{Z}_1} \left(\frac{\sin\left(k_{y1} - \frac{p\pi}{b}\right) h}{\left(k_{y1} - \frac{p\pi}{b}\right)} + \frac{\sin\left(k_{y1} + \frac{p\pi}{b}\right) h}{\left(k_{y1} + \frac{p\pi}{b}\right)} \right) \tag{B.6}$$

$$G_{np} = \frac{1}{\tilde{Z}_2} \langle e_{2,y1n}, \psi_y \rangle = \frac{1}{\tilde{Z}_2} V_{np}$$
$$= \frac{1}{2\tilde{Z}_2} \left(\frac{\sin\left(k_{y2} b - h\left(k_{y2} + \frac{p\pi y}{b}\right)\right)}{\left(k_{y2} + \frac{p\pi y}{b}\right)} + \frac{\sin\left(k_{y2} b - h\left(k_{y2} - \frac{p\pi y}{b}\right)\right)}{\left(k_{y2} - \frac{p\pi y}{b}\right)} \right) \tag{B.7}$$

Bibliography

1. Acton, F.S. *Numerical Methods That Work*. Harper & Row, Washington, D.C., 2nd edition, 1990.
2. Arfken, G.B. and H.J. Weber. *Mathematical Methods for Physicists*. Elsevier Academic Press, New York, NY, 6th edition, 2005.
3. Baker-Jarvis, J., E.J. Vanzura, and W.A. Kissick. "Improved Technique for Determining Complex Permittivity with the Transmission/Reflection Method." *IEEE Transactions on Microwave Theory and Techniques*, 38(8):1096–1103, August 1990.
4. Balanis, C. *Advanced Engineering Electromagnetics*. John Wiley & Sons, Inc., New York, NY, 1989.
5. Beckett, R. and J. Hurt. *Numerical Calculations and Algorithms*. McGraw-Hill Book Company, New York, NY, 1967.
6. Berk, A.D. "Variational Principles for Electromagnetic Resonators and Waveguides." *IRE Transactions on Antennas and Propagation*, 105–111, April 1956.
7. Bogle, A. E. *Electromagnetic Material Characterization using a Partially Filled Rectangular Waveguide*. Master's thesis, Michigan State University, Lansing, Michigan, 2004.
8. Catala-Civera, J. M., F. L. Penaranda-Foix A. J. Canos, and E. de los Reyes Davo. "Accurate Determination of the Complex Permittivity of Materials With Transmission Reflection Measurements in Partially Filled Waveguides." *IEEE Transactions on Microwave Theory and Techniques*, 51(1):16–24, January 2003.
9. Champlin, K.S. and G.H. Glover. ""Gap Effect" in Measurement of Large Permittivities." *IEEE Transactions on Microwave Theory and Techniques*, 397–398, August 1966.
10. Collin, R. E. *Field Theory of Guided Waves*. IEEE Press, New York, NY, 2nd edition, 1991.
11. Collin, R.E. and R.M. Vaillancourt. "Application of Rayleigh-Ritz Method to Dielctric Steps in Waveguide." *IRE Transactions on Microwave Theory and Techniques*, 177–184, July 1957.
12. Dorey, S. P. *Stepped Waveguide Electromagnetic Material Characteriz ation Technique*. Master's thesis, Graduate School of Engineering, Air Force Institute of Technology (AETC), WPAFB, Ohio. AFIT/GEO/ENG/04-01, 2004.
13. Fehlen, R. G. *Air Gap Error Compensation for Coaxial Transmission Line Method of Electromagnetic Material Characterization*. Master's thesis, Graduate School of Engineering, Air Force Institute of Technology (AETC), WPAFB, Ohio. AFIT/GE/ENG/06-20, 2006.

14. Gardiol, F. E. "Higher Order Modes in Dielectrically Loaded Rectangular Waveguides." *IEEE Transactions on Microwave Theory and Techniques*, 16(11):919–924, November 1968.

15. Gonzalez, G. and D. C. Stinson. "Propagation in Rectangular Waveguide Partially Filled with an Inhomogeneous Dielectric." *IEEE Transactions on Microwave Theory and Techniques*, 284–286, May 1969.

16. Harrington, R. F. *Time-Harmonic Electromagnetic Fields*. IEEE Press, New York, NY, 2001.

17. Havrilla, M. J. *Analytical and Experimental Techniques for the Electromagnetic Characterization of Materials*. Ph.D. thesis, Michigan State University, Lansing, Michigan, 2001.

18. Hyde, M. W. *Determining the Resistivity of Resistive Sheets using Transmission Measurements*. Master's thesis, Graduate School of Engineering, Air Force Institute of Technology (AETC), WPAFB, Ohio. AFIT/GE/ENG/06-24, 2006.

19. Jarem, J. M., J. B. Johnson Jr., and W. S. Albritton. "Measuring the Permittivity and Permeability of a Sample at K_a Band using a Partially Filled Waveguide." *IEEE Transactions on Microwave Theory and Techniques*, 43(12):2654–2667, December 1995.

20. Knott, E. F., J. F. Shaeffer, and M. T. Tuley. *Radar Cross Section*. SciTech Publishing, Inc., 2nd edition, 2005.

21. L.F.Chen, C.K. Ong, C.P. Neo, V.V. Varadan, and V.K. Varadan. *Microwave Electronics*. John Wiley & Sons, Ltd, 2004.

22. Marcuvitz, N. *Waveguide Handbook*. McGraw-Hill Book Company, Inc, 1951.

23. Nicolson, A.M. and G.F. Ross. "Measurement of the Intrinsic Properties of Materials by Time-Domain Techniques." *IEEE Transactions on Instrumentation and Measurement*, 19:377–382, November 1970.

24. Pozar, D. M. *Microwave Engineering*. John Wiley & Sons, Inc, 6th edition, 2005.

25. Taylor, John R. *An Introduction to Error Analysis*. University Science Press, Sausalito, CA, 2nd edition, 1997.

26. Vorst, A.S. Vander and R.J.M. Govaerts. "Application of a Variation-Iteration Method to Inhomogeneously Loaded Waveguides." *IEEE Transactions on Microwave Theory and Techniques*, 18(8):468–475, August 1970.

27. Weir, W.B. "Automatic Measurement of Complex Dielectric Constant of Permeability at Microwave Frequencies." *Proceedings of the IEEE*, 62(1):33–36, January 1974.

28. Wexler, Alvin. "Solution of Waveguide Discontinuities by Modal Analysis." *IEEE Transactions on Microwave Theory and Techniques*, 15(9):508–517, September 1967.

29. Wilson, Scott B. "Modal Analysis of the "Gap Effect" in Waveguide Dielectric Measurements." *IEEE Transactions on Microwave Theory and Techniques*, 36(4):752–756, April 1988.

REPORT DOCUMENTATION PAGE

Form Approved
OMB No. 0704–0188

1. REPORT DATE *(DD–MM–YYYY)*	2. REPORT TYPE	3. DATES COVERED *(From — To)*
21–03–2007	Master's Thesis	Sept 2005 — Mar 2007

4. TITLE AND SUBTITLE

Material Characterization Improvement
In
High Temperature Rectangular Waveguide Measurements

5a. CONTRACT NUMBER

DACA99–99–C–9999

5b. GRANT NUMBER

5c. PROGRAM ELEMENT NUMBER

6. AUTHOR(S)

Eric A. Buschelman, Second Lieutenant, USAF

5d. PROJECT NUMBER

5e. TASK NUMBER

5f. WORK UNIT NUMBER

7. PERFORMING ORGANIZATION NAME(S) AND ADDRESS(ES)

Air Force Institute of Technology
Graduate School of Engineering and Management
2950 Hobson Way
WPAFB OH 45433-7765

8. PERFORMING ORGANIZATION REPORT NUMBER

AFIT/GE/ENG/07-05

9. SPONSORING / MONITORING AGENCY NAME(S) AND ADDRESS(ES)

AFRL/SNS Material Measurement Lab
Attn: Dr. Peter Munk (peter.munk@wpafb.af.mil)
2591 K Street, BLDG 254
Wright-Patterson Air Force Base, OH 45433-7602 DSN: 785-0279

10. SPONSOR/MONITOR'S ACRONYM(S)

AFRL/SNS

11. SPONSOR/MONITOR'S REPORT NUMBER(S)

12. DISTRIBUTION / AVAILABILITY STATEMENT

Approval for public release; distribution is unlimited.

13. SUPPLEMENTARY NOTES

14. ABSTRACT

This research presents a method by which electromagnetic characterization of materials in a partially filled waveguide can be accurately performed. Higher order modes are excited by the geometry, which are not accounted for in most algorithms. A correction must consider the power transmitted by higher-order modes. Modal solutions, using reference plane independence, for a single top air gap between the material sample and the waveguide wall also presented. Characterization is performed on samples of acrylic and rubberized magnetic radar absorbing material. Calculation of the complex permittivity and permeability of shielding material, within 10% of the true value, was achieved by using less than 15 modes. Improvement of real permittivity is the strongest feature of the algorithm. The inclusion of the reference plane independence analysis greatly improves the level of performance. Results are presented in S-band and X-band.

15. SUBJECT TERMS

partially filled waveguide, reference plane independence, characterization, radar absorbing materials, guided waves, transmission, reflection, mode-matching

16. SECURITY CLASSIFICATION OF:			17. LIMITATION OF ABSTRACT	18. NUMBER OF PAGES	19a. NAME OF RESPONSIBLE PERSON
a. REPORT	b. ABSTRACT	c. THIS PAGE			Michael J. Havrilla
U	U	U	UU	97	19b. TELEPHONE NUMBER *(include area code)* 937-255-3636 × 4582, michael.havrilla@afit.edu